Marine Biology (2024) 171:231
https://doi.org/10.1007/s00227-024-04552-w

ORIGINAL PAPER

Microstructures, crystallography and growth patterns of serpulid tubeworms (Class Polychaeta)

Christian Grenier[1] · Katarzyna Berent[2] · Alejandro Rodríguez-Navarro[3] · Olev Vinn[4] · Antonio G. Checa[1]

Received: 13 May 2024 / Accepted: 21 October 2024

Abstract

Serpulid polychaetes are marine worms that secrete calcium carbonate tubes in which they live. Despite extensive previous research on their microstructures, there are no crystallographic data and their biomineralization process remains unclear. Here, the microstructures of the tubes of seven serpulid species were studied, including their chemical composition, mineralogy and crystallography, using X-ray diffraction, Raman and Fourier transform infrared spectroscopy, scanning electron microscopy, energy dispersive X-ray spectroscopy, focused ion beam, electron backscatter diffraction, and thermogravimetric analysis. Generally, serpulid tubes have a high amount of organic matter (~7.5 wt%), consisting of chitin and proteins, and the calcite is always present as medium to high magnesium calcite. Three main microstructures were identified: granular-prismatic and lamello-fibrillar calcite, and fibrous aragonite. They all displayed an axial texture, which is stronger in the lamello-fibrillar calcite, with the c-axis aligned with the elongation axis of the crystals. These findings demonstrate that only some instances of the granular-prismatic and the lamello-fibrillar calcite are biogenic (primary) microstructures. Conversely, other instances of the granular-prismatic calcite and the fibrous aragonite are a consequence of a recrystallization process (i.e. secondary). Replacement may occur on either primary or secondary calcitic microstructures (replaced by aragonite). Secondary microstructures retain remnants of the previously replaced microstructures, such as vestigial crystals or major growth increments. The high-Mg nature of the calcite favors recrystallization. The plywood arrangement of the lamello-fibrillar calcite is hypothesized to result from the ordering of a chitin fibrillar precursor into a cholesteric liquid crystal phase, with the calcite subsequently growing by oriented nucleation onto the organic fibrils.

Keywords Serpulids · Microstructures · Biomineralization · Crystallography · Episodic growth · Recrystallization

Introduction

The family Serpulidae comprises a diverse group of sedentary marine tubeworms that belong to the class Polychaeta (phylum Annelida). The current number of known serpulid species is 568 (WoRMS Editorial Board 2024). They are widely distributed, from shallow to deep waters (ten Hove and Kupriyanova 2009; Kupriyanova et al. 2014). Except for the sabellid genus *Glomerula* and some cirratulid species, Serpulidae is the only polychaete family in which

Communicated by J. Grassle .

✉ Antonio G. Checa
acheca@ugr.es

Christian Grenier
chgrenier@ugr.es

Katarzyna Berent
kasia.berent@gmail.com

Alejandro Rodríguez-Navarro
anava@ugr.es

Olev Vinn
olev.vinn@ut.ee

[1] Departamento de Estratigrafía y Paleontología, Universidad de Granada, Granada 18071, Spain

[2] Academic Centre for Materials and Nanotechnology, AGH University of Krakow, Kraków 30-059, Poland

[3] Departamento de Mineralogía y Petrología, Universidad de Granada, Granada 18071, Spain

[4] Department of Geology, Institute of Ecology and Earth Sciences, University of Tartu, Tartu 50411, Estonia

Published online: 09 November 2024

the worms secrete calcium carbonate tubes (Hedley 1958; Fischer et al. 2000; Vinn et al. 2008a; Vinn 2009). They are commonly known as "feather duster worms" because of their characteristic organ for suspension feeding and respiration called the radiolar crown, which can be completely retracted inside the tube (Tilic et al. 2021).

Because of their ability to attach to hard substrates and their ecological success (Kupriyanova et al. 2016), serpulids contribute to biofouling (Lacoste and Gaertner-Mazouni 2015; Charles et al. 2018), along with other sessile organisms (such as sponges, barnacles, bryozoans, calcareous algae, or sedentary bivalves). They also play an important ecological role in structuring diverse marine ecosystems. They provide new habitats for other species by occasionally building reefs, thus promoting biodiversity (Rossbach et al. 2021). Serpulids contribute significantly in terms of biomass productivity and sediment formation, acting as carbon sinks (Montefalcone et al. 2022). They are useful as metal pollution indicators (Xie et al. 2005) and anthropogenically induced hypoxic event markers (Jewett et al. 2005). Serpulids are vulnerable to ocean acidification, which adversely alters the biomechanical properties (hardness and elasticity) of the tube structure (Chan et al. 2012).

Serpulids reproduce sexually and generate a trochophore larva, which metamorphoses into a juvenile stage that settles on the substrate (Nelson et al. 2017). The secretion of the tube begins a few days after settlement (e.g., 5 d in *Galeolaria hystrix*, Nelson et al. 2017). Calcification takes place in the neck folds (peristomial collar), situated just below the radiolar crown, where the calcium-secreting tubular-racemose glands are located. These are surrounded by a secretory epithelium composed of mucus cells (Hedley 1956). A mix of calcium carbonate precursors within an organic matrix is secreted and deposited at the growing edge of the tube.

Serpulid tubes are made of either calcite, aragonite, or both (Lowenstam 1954; ten Hove and Van den Hurk 1993; Vinn et al. 2008b, c). Although the mineralogy of most species is unknown, the majority of serpulids studied are calcitic (around 40%), followed by bimineralic (36%) and aragonitic (24%) (Smith et al. 2013). Calcite is always medium- to high-Mg calcite (7–15 wt% $MgCO_3$) (Smith et al. 2013). The tubes have frequent organic membranes marking different growth increments (Vinn 2011). The organic fraction can be separated into soluble and insoluble organic matter, which are mainly composed of carboxylated and sulphated polysaccharides (Tanur et al. 2010).

Since the second half of the 20th century, the microstructures of serpulids have been studied by different authors (Hedley 1958; Weedon 1994), who described lath-like crystals arranged in ordered and disordered chevron layers and locally distributed spherulitic prismatic structures. However, the most extensive research about the ultrastructure and mineral composition of serpulid tubes was conducted by Vinn et al. (2008b), who analyzed 44 recent species from 36 genera. From SEM images, they described a total of twelve different microstructures based on the mineralogy, morphology, and arrangement of the constituting crystals (Table 2 in Vinn et al. 2008b). They distinguished fibrillar, prismatic, platy, and spherulitic microstructures, each arranged in oriented, semi-oriented, or disoriented manners. Other studies also focused on the transitions between microstructures across the different layers of the tube. For instance, Buckman (2015) described in *Spirobranchus triqueter* a progressive change from well-ordered inner and medium layers (chevron layer), constituted by the lamello-fibrillar microstructure, to an outer, less structured layer (pseudo-laminar layer), consisting of the irregularly oriented-prismatic microstructure. In summary, in recent decades, the tube structure of serpulids has been described in detail, resulting in a wide variety of microstructures (fifteen until now), which suggests that serpulids possess a more advanced biomineralization system than previously thought (Vinn 2021).

Unlike other groups of biocalcifiers (e.g. molluscs, Checa and Salas 2017; corals, Coronado et al. 2019; brachiopods, Yin et al. 2021; Simonet Roda et al. 2022), there are no studies on the crystallography of serpulid tubes. In the present study, we analyze the microstructures of seven serpulid species: *Crucigera websteri*, *Spirobranchus triqueter*, *Serpula vermicularis*, *Spirobranchus giganteus*, *Serpula crenata*, *Crucigera zygophora*, and *Floriprotis sabiuraensis*. We determined the existence of only three main types: granular-prismatic and lamello-fibrillar calcite, and fibrous aragonite. For each microstructure, we examined the mineralogy, the type and arrangement of crystallites, their location within the tube, and, for the first time, their crystallographic arrangement.

Materials and methods

Material

Seven serpulid species were analyzed in the present study: *Crucigera websteri*, *Crucigera zygophora*, *Floriprotis sabiuraensis*, *Serpula vermicularis*, *Serpula crenata*, *Spirobranchus giganteus* and *Spirobranchus triqueter*. Available data on collection localities, depths, and dates are provided in Table 1. Specimens were all collected alive, either by hand from intertidal zones, or through diving, trawling, or dredging in the subtidal zone. They were initially preserved in unbuffered 4% formaldehyde solution and subsequently relocated to 70% ethanol for archival storage in museum collections (initially at the Zoological Museum,

Table 1 List of species studied indicating location, depth and date of collection. All species are accepted species according to WoRMS Editorial Board (2024)

Samples	Location	Depth	Date of collection
Subfamily Serpulinae: Tribe Serpulini			
Crucigera websteri	Shelf of Surinam (06°56.6 N, 55°56.9' W)	60–62 m	1966
Crucigera zygophora	Canoe Bay, Alaska, USA	12–40 m	17/09/1970
Floriprotis sabiuraensis	Amakusa, Shimoshima Island, Japan,	< 20 m	30/11/1993
Serpula vermicularis	Loch Creran, Scotland	2–20 m	28/06/2004, 02/07/2004
Serpula crenata	Indonesia, Siboga Expedition (00°59.1' S, 129°48.8' E)	411 m	16/08/1899
Subfamily Serpulinae: Tribe Ficopomatini			
Spirobranchus giganteus	Curaçao, Antilles, The Netherlands	4–6 m	21/05/1970
Spirobranchus triqueter	Tjärnö, Sweden Galicia, NW Spain	Subtidal < 12 m	-- 2021–2022

Amsterdam, and later at the Naturalis Biodiversity Center, Leiden). Specimens were washed and stored dry prior to their study by Vinn et al. (2008b).

Mussels with attached *Spirobranchus triqueter*, from mussel rafts, were purchased at Granada fish markets. Specimens were cleaned, oven-dried and stored.

Scanning electron microscopy (SEM)

Fragments of each of the seven species were cleaned by immersion in commercial bleach (~5% active chlorine) for 2 h while stirring. Then, the bleach solution was removed by several ultrasonication washes (2–3 min each) in deionized water. Once oven-dried at 40 °C for 24 h, the fragments were embedded in epoxy resin (EpoFix, Struers). After 48 h of hardening, a cross-section of each tube was exposed by successive grinding steps with 360, 600, 1200, and 3000 (ANSI/CAMI US grit numbers) electroplated diamond discs. Subsequently, the surfaces were polished with high-density wool felt pad discs (adding 1 µm and 0.25 µm of polycrystalline diamond suspension, Struers), until reaching a mirror surface finish. A Hi-Tech Diamond polishing machine (All-U-Need model) was used for both grinding and polishing. Finally, an etching and decalcifying solution (2.5% glutaraldehyde, 0.25 M HEPES buffer, and 0.05 M EDTA) was applied directly to the exposed surfaces for 1 min in a stirring module. SEM observations were performed after carbon coating (Emitech K975X carbon evaporator) using Secondary Electron (SE) and BackScatter Electron (BSE) detectors in a field emission SEM FEI QemScan 650 F and a Carl Zeiss SMT AURIGA Crossbeam Station. All the equipment is housed in the Centro de Instrumentación Científica (CIC) at the Universidad de Granada (UGR).

Raman microscopy

Analyses were performed on the samples prepared for SEM after repolishing to remove the carbon coating. A dispersive Micro-Raman spectrometer (JASCO NRS-5100/7000 Series) was used. The light source used was a VIS-NIR red diode that generated a laser beam at 785.11 nm with a spot size of 4 µm. The spectrum analyzed ranged from 100 cm^{-1} to 1200 cm^{-1}, with a data interval of 1 cm^{-1}. The exposure time was 20 s, with five accumulations per measurement and a resolution of 6.49 cm^{-1}. All the measurements were taken with the 20x objective at a degree of laser attenuation (aperture) O.D. -1 and with corrected fluorescence. Software Spectra Manager II was used for system control, data acquisition, and data analysis. Analyses were carried out at the Centro de Instrumentación Científica (CIC) of the University of Granada (UGR).

X-ray diffraction (XRD) and Rietveld refinement

We only used the species *Serpula vermicularis* and *Spirobranchus triqueter* due to material availability. Cleaned tube fragments from both species were ground to a fine powder and heated to 25 °C, 200 °C and 400 °C in an oven. The samples were analyzed with an X-ray powder diffractometer (PANalytical X'Pert PRO) at the Department of Mineralogy and Petrology, University of Granada, using Cu radiation ($\lambda = 1.5406$Å). The data were collected in reflection mode, from 4° to 120° (°2θ) with a step size of 0.017° and 69.85 s integration time per step. Rietveld refinement analyses of XRD profiles were done using TOPAS 5.0 software (Bruker, Germany) to determine the quantitative mineral concentration (at 25 °C). The calcite unit cell parameters were refined to calculate the cationic substitutions (% Mg) in calcite (average of the measurements at each temperature). A small amount of silicon powder was added to the sample as an internal standard to more precisely determine the d-spacings (Dos Santos et al. 2017).

Electron backscatter diffraction (EBSD)

A total of 12 EBSD maps were made on *Serpula crenata*, *Serpula vermicularis*, *Spirobranchus triqueter*, and *Spirobranchus giganteus*. The samples prepared for SEM observation were finished with a manual etch-polishing step (for 3–5 min) by applying alumina suspension (0.3 µm, Buehler).

The samples were coated with 4 to 6 nm of carbon (Leica EM ACE200). Measurements were taken on a FEI Versa 3D scanning electron microscope (SEM) equipped with the Symmetry S2 CMOS-based EBSD detector (Oxford Instruments). The data were acquired using Aztec 6.0 software with an accelerating voltage of 20 kV. EBSD measurements were made in step increments between 20 and 25 nm.

Information obtained from EBSD diffraction measurements was processed by CHANNEL 5 HKL software. The results are presented as band contrast (BC) measurement images, where white or dark regions correspond to higher or weaker signal strengths, respectively, of the EBSD Kikuchi diffraction patterns. The Inverse Pole Figure (IPF) maps are color-coded crystal orientation images, where similar colors indicate similar orientations. The term "texture" relates to the orientation of the crystallographic axes within a material. The texture is represented by the pole figures (PFs) corresponding to each EBSD map. The PFs are presented either as individual data points or as density contours. In the latter case, we used the lowest possible degree for half-width (5°) and cluster size (3°). The half-width controls the extent of the spread of the poles over the surface of the project sphere. A cluster comprises data with the same orientation. We also provide the Multiple of Uniform Distribution (MUD) values. Low MUD values indicate a random orientation or low co-orientation of crystals, while high values indicate high crystal co-orientation. Very high values (MUD > 700) are characteristic of a high-quality, single crystal (i.e., geological calcite of optical quality).

Focused Ion Beam (FIB) and transmission-electron backscatter diffraction (t-EBSD)

Transmission Kikuchi Diffraction (TKD), also known as the t-EBSD technique, was conducted with the same FEI Versa 3D SEM equipment as for EBSD measurements. Ultra-thin lamellae for t-EBSD were prepared on a FEI Quanta 200i SEM (gallium FIB column). The sample surface was coated by FIB deposition with a 2 µm thick protective stripe of tungsten, whose length is equal to that of the lamella to be extracted. Trenches were then excavated on both sides of the deposited layer in two steps: rough milling was performed with a 30 kV 15 nA ion beam, followed by finer milling steps using a 30 kV 1 nA beam current. A thin fragment of the sample was separated from the rest, transferred, and attached to the TEM copper grid by an OmniProbe micromanipulator. Subsequently, the FIB lamella was thinned by Ga ions on both sides at 30 kV, with a beam current initially set at 300 pA, which was gradually reduced to 50 pA. The final thinning step (to ~ 100 nm) was conducted at 5 kV and 50 pA, to minimize surface damage.

Thermogravimetric analysis (TGA)

Cleaned and dried tube fragments were ground to a fine, homogeneous powder. Approximately 20 mg of material were analyzed using a METTLER-TOLEDO (TGA/DSC1) equipment, with a heating rate of 20 °C/min in air. From the TGA curves, the total amounts of water (weight loss from 25 °C to 200 °C), organic matter-I (weight loss from 200 °C to 400 °C, presumably corresponding to intermineral proteins and polysaccharides), and organic matter-II (weight loss from 400 to 600 °C, corresponding to intramineral proteins) were determined for each sample (Rodríguez-Navarro et al. 2006; Rashidi et al. 2012).

Decalcification and Fourier Transform Infrared Spectroscopy (FTIR)

This was only applied to the species *Spirobranchus triqueter*, due to the availability of material. A fragment (1 cm in length) was treated with commercial bleach and then washed several times with sonicated ultrapure distilled water (milli Q). Once oven-dried at 40 °C, the fragment was immersed in a decalcifying solution (0.05 M EDTA + 0.1 M HEPES + 2.5% Glutaraldehyde). The decalcification process was carried out in an orbital shaker for 24 h at room temperature, and the solution was replaced several times. The resulting loose membranes were gently washed several times with ultrapure distilled water (MilliQ) and oven-dried at 40 °C. They were then placed on an attenuated total reflection (ATR) diamond unit (Jasco Pro One) and analyzed by a FTIR spectrometer (Jasco 6600). To calculate the standard deviation and error, four repetitions were performed in different areas of each membrane. The range of the spectrum was 400 cm^{-1} to 4000 cm^{-1}, with a resolution of 2 cm^{-1} and 100 scans. Spectra Manager software was used for system control and data acquisition. IR peaks associated with the main chemical components (i.e., proteins, polysaccharides, carbonates) were measured to determine the chemical composition of the samples.

Results

Microstructures: overview and mineralogy

Based on crystal morphology and arrangements, we identified three main microstructures: (1) granular-prismatic, present as either continuous external layers, discontinuous internal layers or ubiquitous clusters (Fig. 1A, B, E); (2) lamello-fibrillar, constituting the central and internal parts of the tubes (Fig. 1A, C); (3) fibrous spherulites, forming discontinuous internal or external layers or clusters with no

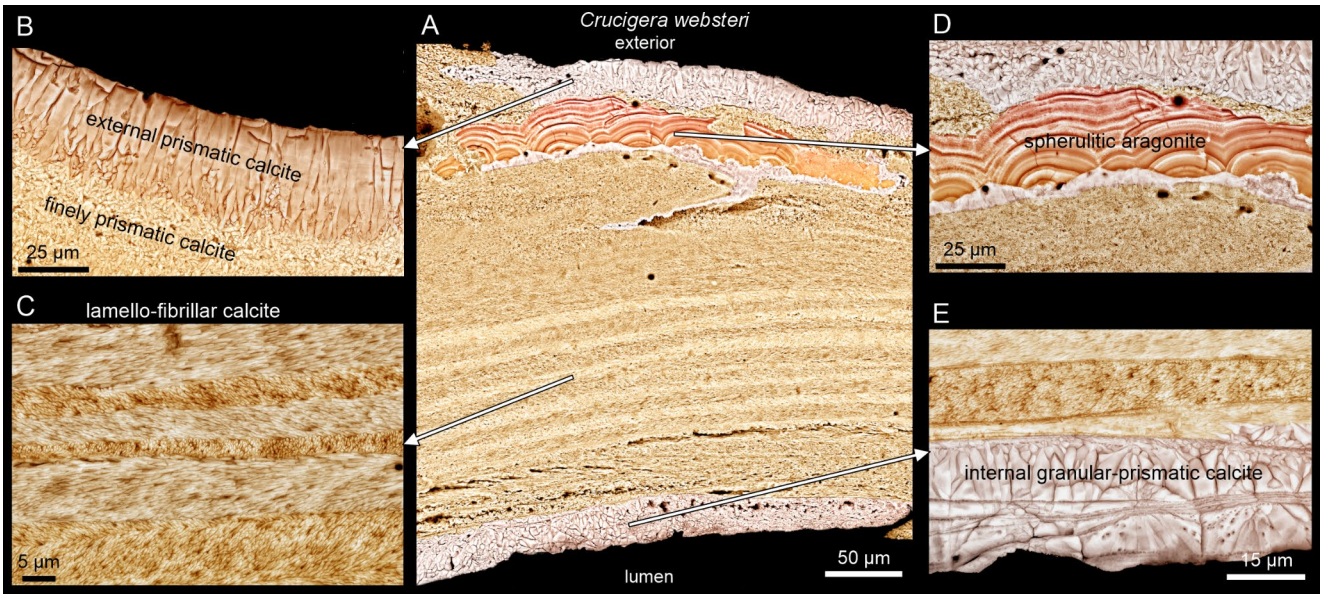

Fig. 1 The three microstructures identified and locations within serpulid tube. (A) Cross-section of tube of *Crucigera websteri* including all microstructures. (B) External prismatic calcite underlain by finely prismatic cacite. (C) Lamello-fibrillar calcite forming most of tube thickness. (D) Cluster of aragonite spherulites. (E) Irregular internal layer of granular-prismatic calcite

preferential location (Fig. 1A, D). With few exceptions, all microstructures appeared in the different species studied.

The mineralogy of the three microstructures was determined by Raman infrared spectroscopy and XRD (Figs. S1 and S2). Calcite presented distinctive Raman peaks at around 1084 cm^{-1}, 710 cm^{-1} and 282 cm^{-1} (Kim et al. 2021), whereas aragonite peaks were at around 1082 cm^{-1}, 702 cm^{-1} and 285 cm^{-1} (Badou et al. 2022).

The granular-prismatic microstructure consisted of calcite, as indicated by the spectra obtained from the outermost layers of *Serpula vermicularis* and *Spirobranchus triqueter* (Fig. S1A and B, respectively), as well as from *Crucigera websteri* and *Serpula crenata* (Fig. S2A, C). The same was true for the lamello-fibrillar layers observed in the middle area of cross sectioned tubes of *S. vermicularis* and *S. triqueter* (Fig. S1A and B, respectively), as well as in *C. websteri*, and *Spirobranchus giganteus* (Fig. S2A, B). The fibrous microstructure was always made of aragonite, as shown by the analyses performed on the inner layers of *S. vermicularis* (Fig. S1A) and *S. giganteus* (Fig. S2B), as well as on the near external spherulitic clusters of *C. websteri* and in the variously positioned spherulites of *S. giganteus* (Fig. S2A and B, respectively).

The percent of magnesium substitution in the calcite was determined by Rietveld refinement of XRD patterns of tube fragments. In the examples analyzed, calcite had a medium (*Serpula vermicularis*) to high magnesium (*Spirobranchus triqueter*) content (Fig. S1C, D).

Granular-prismatic calcite

The granular-prismatic microstructure was present in two different varieties according to their location, and to the shape and arrangement of the grains or prisms (Fig. 2):

1) Outer layers of finely prismatic, disoriented crystals that changed outward into coarse prisms arranged perpendicular to the external surface (Figs. 1A, B and 2A–E). Within the coarse vertical prisms, small intra- and intercrystalline grains, either isolated or clustered, were observed (black arrows in Fig. 2B, C). The layer was usually several tens of microns thick, but could reach hundreds of microns at the ribs of some species (e.g. *Serpula vermicularis* and *Serpula crenata*; Figs. 2E and 3, respectively). While most of the prisms increased in diameter as they grew and reached the outer surface, others tended to disappear at the earliest stages (Figs. 1A and 2A–C). They presented growth lines parallel to their flat outer surfaces, which were continuous across adjacent prisms (arrowheads in Fig. 2A, and white arrows in Fig. 2D). In some areas, the prisms presented arrowhead endings and similarly shaped growth lines (Fig. 2C, D, black arrows), which correspond to rhombohedral faces in 3D view (Fig. 2C). Under high magnification, the crystal surface nano-roughness was appreciated (insets in Fig. 2C, D).

2) Irregular layers or aggregates close to or at the innermost part of the tube (Figs. 1E and 2F–J), which laterally changed into the layers of the lamello-fibrillar microstructure (Fig. 2F, I). The prisms-grains ranged from < 1 one to several 10s of microns both in length and thickness. Vestiges

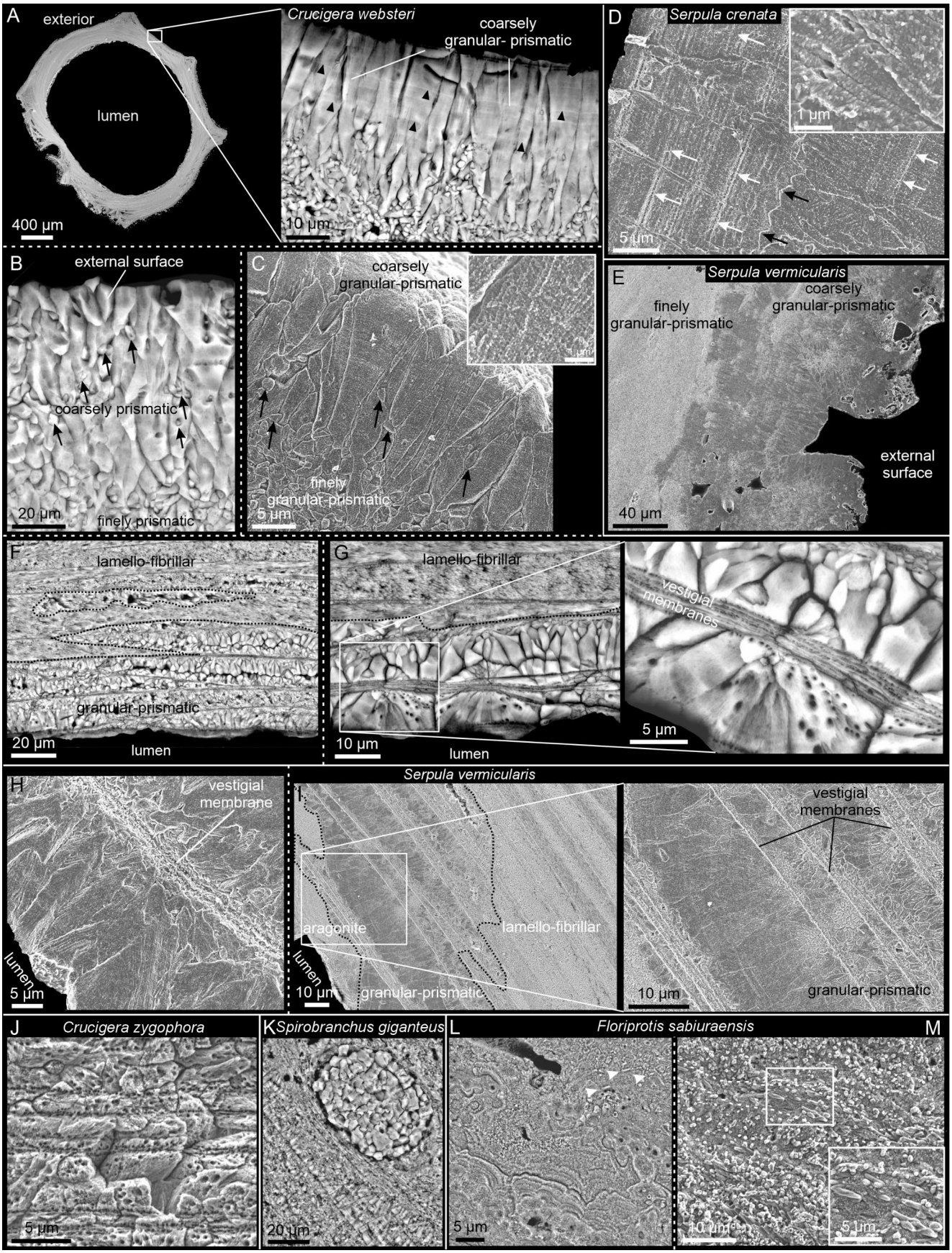
A
exterior
lumen
400 µm
Crucigera websteri
coarsely
granular- prismatic
10 µm
D
Serpula crenata
1 µm
5 µm
B
external surface
coarsely prismatic
20 µm
finely prismatic
C
coarsely
granular-prismatic
finely
granular-prismatic
5 µm
E
Serpula vermicularis
finely
granular-prismatic
coarsely
granular-prismatic
external
surface
40 µm
F
lamello-fibrillar
granular-prismatic
20 µm
lumen
G
lamello-fibrillar
10 µm
lumen
vestigial
membranes
5 µm
H
vestigial
membrane
lumen
5 µm
Serpula vermicularis
I
aragonite
lamello-fibrillar
lumen
10 µm
granular-prismatic
vestigial
membranes
10 µm
granular-prismatic
J
Crucigera zygophora
5 µm
K
Spirobranchus giganteus
20 µm
L
Floriprotis sabiuraensis
5 µm
M
10 µm
5 µm

Fig. 2 Granular-prismatic calcite. (A-C) External layers with granular-prismatic microstructure of *Crucigera websteri*. (A) Cross-section of tube of and external layer. Innermost part of layer formed by fine, disordered prismatic crystals, which change into coarse prisms arranged perpendicular to external surface. Parallel growth lines extend between adjacent prisms (arrowheads). (B) Same external granular-prismatic layer as in A, showing small grains within and between prisms (black arrows). (C) Prisms arranged perpendicular to outer surface, exhibiting rhombohedral endings. Arrows point to inter- and intra-prismatic small grains. Surface nano-roughness can be appreciated (inset). (D) External granular-prismatic calcite of *Serpula crenata.* Prisms perpendicular to external surface. Straight and parallel growth lines continuous across adjacent prisms (white arrows). Some prisms at the bottom show arrowhead endings (black arrows). Surface nano-roughness visible (inset to top). (E) External granular-prismatic calcite of *Serpula vermicularis*, forming layers with very irregular outlines. (F-I) Internal granular-prismatic layers in *C. websteri* (F and G) and *S. vermicularis* (H and I). Smaller, disoriented prisms nucleate on vestiges of organic membranes between lamello-fibrillar layers penetrating prismatic-granular layers (particularly evident in G and H). (J) Irregularly sized prisms growing across vestigial membranes in *Crucigera zygophora*. (K) Lamello-fibrillar layer of *Spirobranchus giganteus*, including prismatic layers (bottom left part) and a central concretion of granular calcite, with fibers adapting to its lower contour. (L, M) Two examples of granular-prismatic microstructure in *Floriprotis sabiuraensis* with residual co-oriented fibers (arrowheads). (L) Irregular concretionary growth front within granular-prismatic layer. (M) Granular-prismatic mass containing sparse or clustered smaller fibers, co-oriented and distributed in layers (one such layers indicated by broken lines). Their sizes and mode of co-orientation are typical of the lamello-fibrillar microstructure

of the organic membranes separating the lamello-fibrillar layers continued into the granular-prismatic microstructure. The grains-prisms usually nucleated on the vestigial membranes (Fig. 2F–I), sometimes forming spherulites with well-defined concentric growth lines, which indicated radial growth (detailed view in Fig. 2G). The prisms sometimes continued across the vestigial membranes (Fig. 2J). Microborings cutting through the prism growth lines were occasionally present (Fig. 2G, J). Exceptionally, round aggregates of granular calcite were found within lamello-fibrillar layers (Fig. 2K). On occasions, the spherulites fused to form continuous, irregular, concretion-like growth fronts (Fig. 2L). In other instances, the granular-prismatic material constituted a matrix, which contained co-oriented isolated fibers or clusters of them, typical of the lamello-fibrillar microstructure (Fig. 2M).

The crystallography of the granular-prismatic calcite, particularly the coarse prisms of the external layer, is shown in Figs. 3 and S3. The EBSD maps showing the mineral distribution and crystal orientation were done on a ridge of *Serpula crenata*, made entirely of granular-prismatic calcite. The BC map of Fig. 3A depicted well indexed areas on both sides of the ridge, but not in the dark central region, where the diffraction signal was either too weak or absent. The phase maps corroborated that the entire ridge consisted of calcite (Figs. 3B and S3B). While the prisms of Fig. 3 were sectioned parallel to their long axes, those of Fig. S3 were sectioned oblique to their axes. The IPFz map of Fig. 3C revealed a predominance of green-purple colors, which suggested that the prisms had their c-axes in plane (see the triangle color key). The PFs are plotted for three separate regions (two lateral and one central) (Fig. 3C). Both raw and contoured PFs displayed a well-defined axial texture, which was better defined in the lateral regions. The calcite c-axis coincided with the elongation axis of the prisms (Fig. 3C) and remained at a high angle to the external surface (as indicated by the unit cells), adapting to the change in curvature of the ridge. The MUD value of the top lateral region was significantly higher (69) than those of the central (27) and bottom lateral (32) regions, coinciding with the greater spread of the c-axes in the latter regions. Their low MUD values could be attributed to the scarcity of indexed points. To check the change in co-orientation of the prisms with growth, we cropped three regions of the top area belonging to the progressive developmental stages of the prisms (Fig. 3D). There was a reduction in the dispersion of the maxima in the contour PFs and an increase of the MUD values (from 40 to 60 to 76), indicating that prisms became progressively co-oriented with growth. The EBSD map of Fig. S3 provided similar results. The IPF map displayed a wider range of colors and the maxima for the c-axes were displaced from the center due to the oblique cut (Fig. S3C). The subsets indicated that the MUD values also increased from the interior to the exterior (Fig. S3D), although the bottom subsets displayed lower values because the higher curvature of the area (indicated by the growth lines; Fig. S3A) gave rise to a higher dispersion of the c-axes. An additional EBSD crystal orientation map was performed directly on the polished surface of the transverse cross-section of the *Spirobranchus giganteus* tube (Fig. S4). The area analyzed contained several layers of granular-prismatic calcite delineated by vestigial membranes in the middle of the tube (Fig. S4A–C). The prisms were, in general, oriented perpendicular to the membranes. As in the previous instances, the IPFz map and the PFs indicated that the calcite c-axes were in plane (Fig. S4D) and parallel to the elongation axes of prisms. It had a weak axial texture (MUD value 23). This arrangement was particularly evident in the central layer (delimited by white broken lines in Fig. S4D), which consisted of coarse prisms (see cell lattices). It displayed a medium axial texture (MUD value 56).

The crystallographic data for the finely granular-prismatic calcite underlying the coarse granular prismatic calcite are provided in Fig. 4. The EBSD map was performed in a longitudinal cross-section of a *Serpula crenata* tube, similar to that in Fig. 4A. The BC map (Fig. 4B) showed a stronger diffraction signal for the coarse prisms. The phase map confirmed the calcitic composition of the

microstructure (Fig. 4C). The wide variety of colors of the IPFz map of the finely prismatic grains (top right of map in Fig. 4D) indicated that their axes are not co-oriented (see cell lattices). The PFs corroborated the lack of texture, with scattered maxima for all axes and a very low MUD value (9). Conversely, the overlying coarse prisms presented a predominance of green-purple colors (bottom left of map in Fig. 4D), which meant that they were co-oriented (as also indicated by the cell lattices), with the c-axis along their elongation axes and almost in plane. The coarse prisms had a moderate axial texture (MUD value 56), with the c-axis as the fiber axis.

Lamello-fibrillar calcite

The lamello-fibrillar microstructure was made of superposed layers of thin, elongated, and co-oriented calcite fibers, arranged parallel to the growth surfaces (Figs. 1A, C and 5). Conspicuous organic membranes separated the layers (magnifications in Fig. 5A–C) and organic threads were present between the calcite fibers (arrowheads in Fig. 5A, C). The layers were not homogeneous in thickness, varying from 2 to more than 10 µm in width (Figs. 1C and 5A–E), and they frequently wedged out laterally (Fig. 5F, G). Fiber size ranged from 3 to 6 µm in length and 400–600 nm in width. Fibers of single layers were strictly co-oriented, although some particularly thick layers showed a progressive twisting across the layer thickness (white arrows in Fig. 5A, D). There was always a noticeable change in orientation between superposed layers (Figs. 1C and 5A, C, D, G). In all samples studied, the lamello-fibrillar microstructure constituted the middle and internal parts of the tube, except for intercalated layers or clusters of granular-prismatic calcite or spherulitic fibrous aragonite (Figs. 1A and 5A, B). As the lamello-fibrillar microstructure approached the outer surface, its organic membranes reflected back (Fig. 5B) at the same time that it changed into the disordered, non-layered finely granular-prismatic microstructure (Fig. 5A, B).

Crystallographic data on the lamello-fibrillar microstructure of *Spirobranchus triqueter* and *Serpula vermicularis* (Fig. 6) were obtained with t-EBSD. Maps were either parallel (Fig. 6) or perpendicular (Fig. S5) to the longitudinal direction of the fibers within single layers (see lamellae preparation in Fig. S6). The BC map of *S. triqueter* (Fig. 6A) showed well-defined fiber contours, indicating a good EBSD diffraction signal for the entire lamella, whereas for *S. vermicularis*, the BC map showed gaps in the left area due to damage by ion beam during sample preparation (dark area in Fig. 6D). In *S. triqueter*, the fibers were arranged in two different directions: longitudinally at the top and transversely at the bottom. In *S. vermicularis*, the fibers were co-aligned in a single layer although there was some spread of the axes. The phase maps corroborated that the only phase was calcite (Fig. 6B, E). The EBSD color maps (IPFz maps, Fig. 6C, F) revealed a predominance of green-purple colors for the longitudinally cut fibers and reddish for the transversally cut fibers. This indicated that, in the first instance, the fibers had been cut close to their c-axis, whereas in the latter case, the c-axes were at a high angle to the image plane (see the triangle color key). The PFs (Fig. 6C, F) displayed a strong axial texture, with the c-axis as the fiber axis (depicted by the unit cells). In *S. triqueter*, the maximum for the c-axis was well-clustered and the MUD values were very high (176 for the longitudinal fibers and 90 for the transverse fibers) (Fig. 6C). In *S. vermicularis*, the c-axis maximum was broader and the MUD value was significantly lower (41) (Fig. 6F), likely due to the progressive change in orientation of the c-axes (see also cell lattices). An additional EBSD map of the lamello-fibrillar calcite of *S. triqueter* was directly performed on the middle part of a polished cross-section (Fig. S7). Three different layers could be distinguished on the BC map (Fig. S7B), with fibers of each layer displaying different orientations and sizes, however all made of calcite according to the phase map (Fig. S7C). The IPFz map and the PFs indicated that the c-axes of most fibers were roughly parallel to the viewing plane in the lateral layers, and at a high angle in the central layer (see also cell lattices for each layer, Fig. S7D). The right layer demonstrated thin and well co-oriented fibers (medium axial texture, MUD value 62), characteristic of the lamello-fibrillar microstructure. In the central and left layers, there was an increase in size and a decrease in co-orientation (MUD values 25 and 31 for the central and left layers respectively), thus being more typical of the granular-prismatic microstructure.

Decalcification with EDTA of the lamello-fibrillar microstructure of *Spirobranchus triqueter* exposed the arrangement of curved organic membranes (Fig. S8A, right), with changes in thickness of the intervening layers similar to those observed in non-decalcified samples (Figs. 6A, B, D, F, G and S8A, left). The thermogravimetric analysis revealed that the total amount of organic matter was ~7.5% of the total weight (weight loss between 200 °C and 600 °C; Fig. S8B). The organic membrane chemical composition obtained by FTIR-ATR analysis indicated that it contained mainly proteins and sulfated polysaccharides (Fig. S8C).

Fibrous aragonite

The fibrous aragonite microstructure consisted of needle-like aragonite fibers, usually arranged into spherulites, where the fibers radiated from a nucleation center, in a fan-like arrangement (Figs. 1A, D and 7). They had rounded (Figs. 1D and 7B–D, G, I, J, K) or, rarely, angular outlines

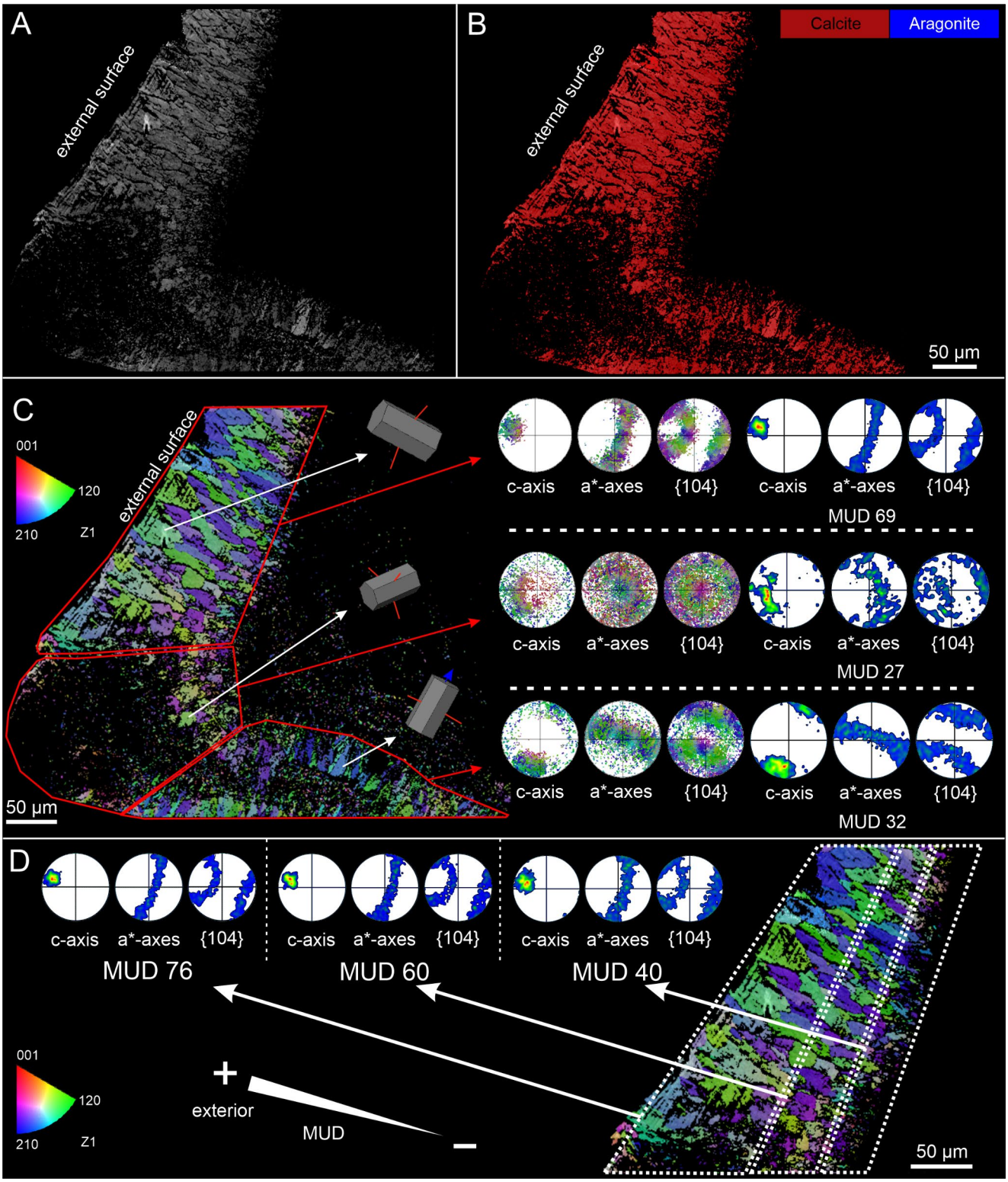

Fig. 3 EBSD analysis of granular-prismatic calcite (coarse prismatic layer) of ridge of *Serpula crenata*. (A) The BC map (grey color) shows central area with weak to absent EBSD diffraction signal (dark area). (B) Phase map indicates that whole structure is made of calcite (see legend). (C) IPFz map of ridge and PFs of three regions differentiated (two lateral and one central). Green-purple colors predominant, indicating that c-axes are in plane. PFs display axial textures (weaker at central region). C-axis roughly perpendicular to external surface and changing in orientation coinciding with curvature of the ridge, as also indicated by unit cells. MUD value of top lateral region higher than values of central and bottom lateral regions. (D) IPFz map of top lateral area of C. Contour PFs are plotted from three different growth stages. There is progressive reduction in spread of maxima of contour PFs toward exterior (from right to left), along with increase of MUD values (from 40 to 76). This indicates that texture becomes stronger with growth. Color triangle is key for orientations

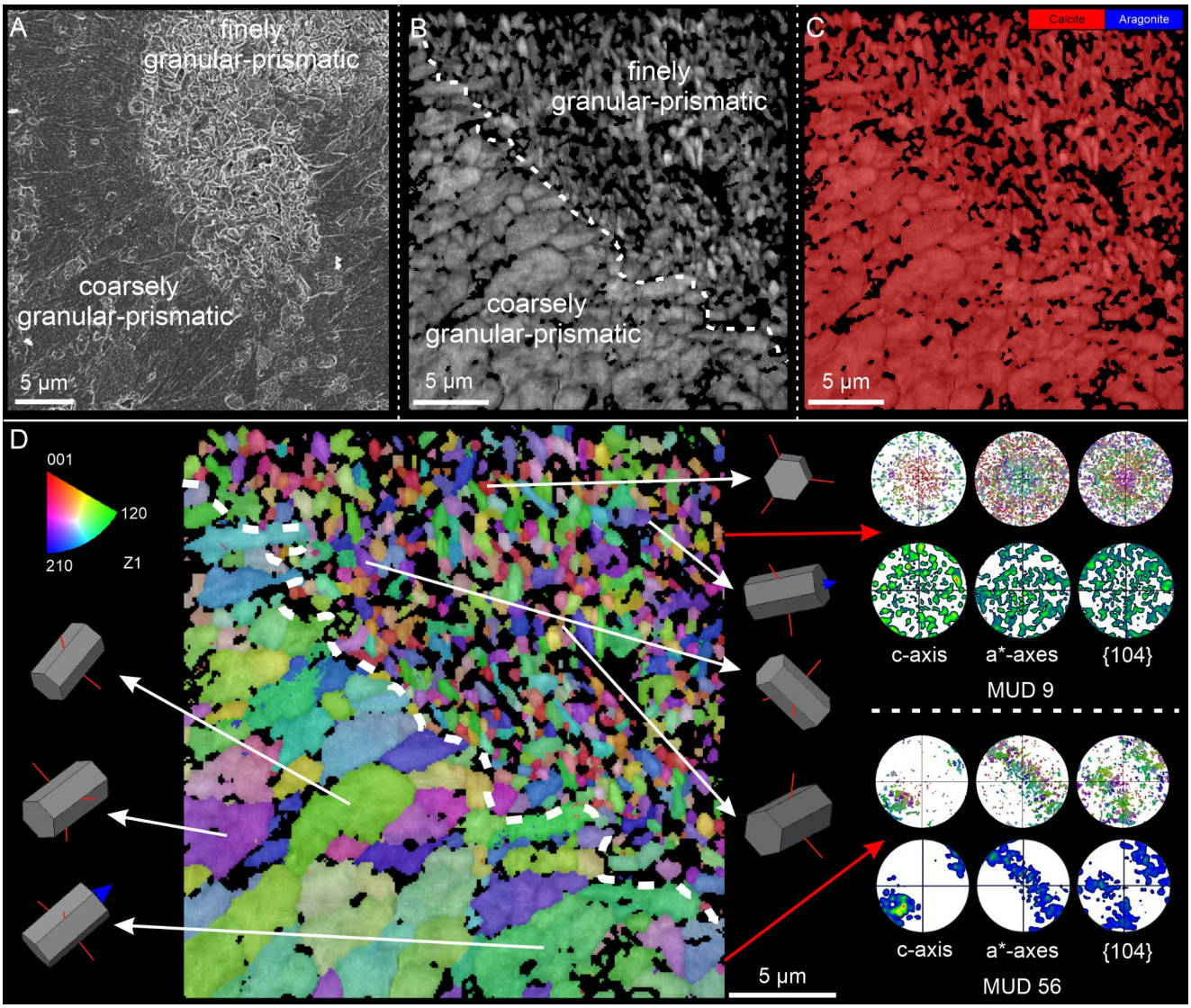

Fig. 4 EBSD analysis of two superposed types of granular-prismatic calcite of *Serpula crenata* (finely and coarsely prismatic), forming outer layer of tube. (A) SEM image of area similar to that analyzed. (B) BC map showing two types of granular-prismatic calcite. (C) Phase map indicating microstructure made of calcite (see legend). (D) IPFz map depicting broader color variation of finely granular-prismatic calcite compared to coarsely prismatic calcite. PFs of finely granular calcite present scattered maxima for all axes, while coarsely prismatic calcite displays moderate axial texture, with c-axis (fiber axis) at a small angle to sectioning plane (also indicated by unit cells). Color triangle is key for orientation

(Fig. 7A). Aragonite spherulites could be found as discontinuous layers of highly variable thickness, either at the innermost or the outermost part of the tube (Figs. 1A and 7A, C, E–H). When internal layers became particularly thick, the growth front of coalescing spherulites may become increasingly flat (Fig. 7C, F). Locally, convex growth lines indicated growth toward either the exterior (Fig. 7C, F) or the interior (Fig. 7G, H). Spherulites could also be found as clusters of variable sizes in any region within the tube (Fig. 7D, E, G, I, J). Then, they exhibited well-defined concentric growth lines (Figs. 7B, D, G, I, J, K and 8), whose convexity indicated growth toward either the exterior of the tube (Fig. 7D, I) or the lumen (Fig. 7B, G, J, K). Fibrous aragonite could be found in contact with either the lamello-fibrillar or the granular-prismatic microstructures. In the first instance, the spherulite growth lines occasionally overprinted the relicts of the membranes between the lamello-fibrillar layers (Figs. 7B, H, J, K and 8C). In a way similar to some internal prismatic microstructures, fibrous aragonite growth lines were frequently traversed by borings (Fig. 7D, F–K). The interface between the aragonitic and calcitic microstructures was further analyzed using EDX in *Spirobranchus giganteus* (Fig. 8), which allowed for the identification of calcite grains according to their Mg^{2+} content (blue color in Fig. 8).

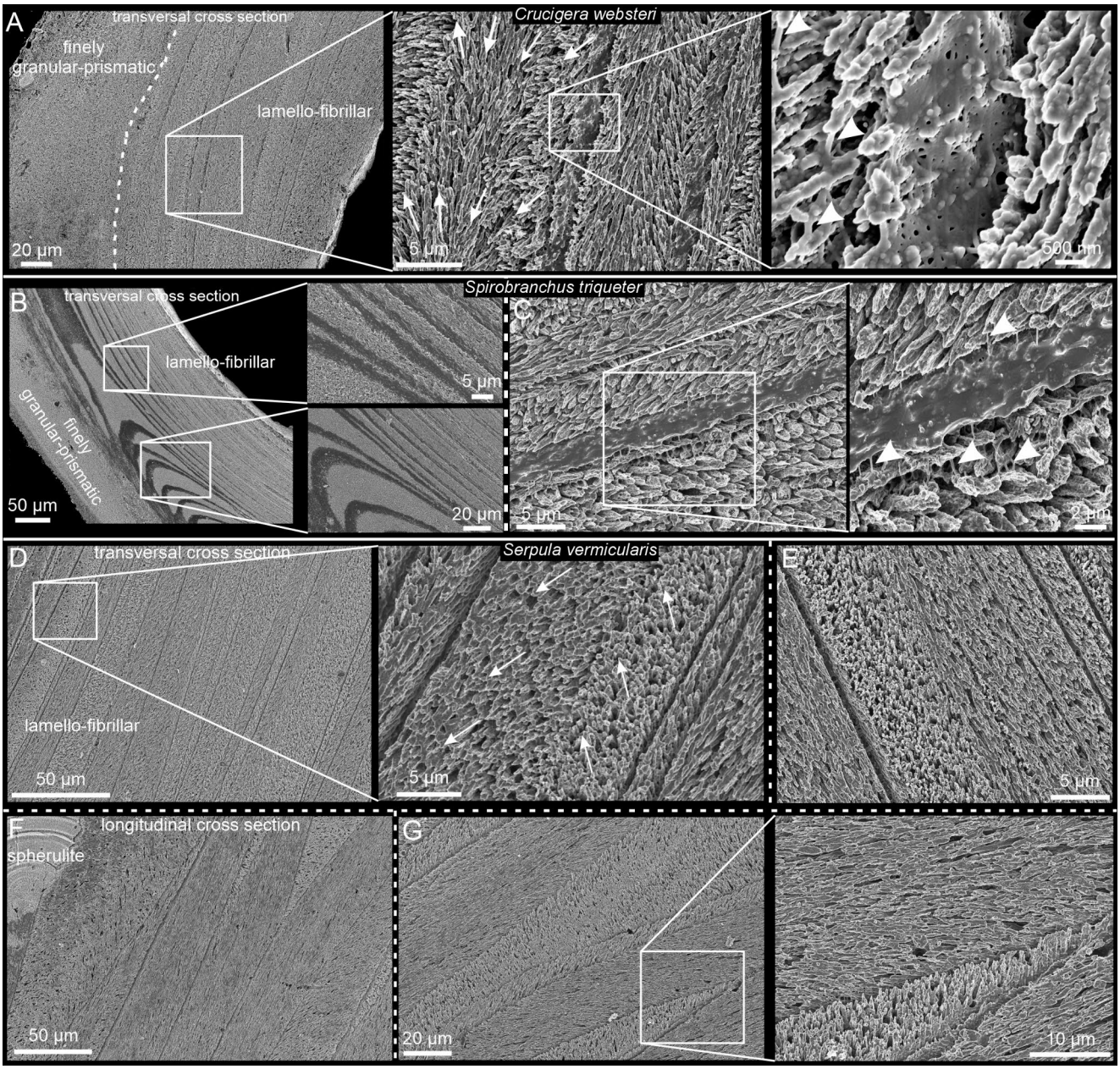

Fig. 5 Lamello-fibrillar calcite of polychaetes. (A) Lamello-fibrillar microstructure of *Crucigera websteri*. Boundary with finely granular-prismatic material indicated. Progressive magnifications show changing orientations of fibers in different layers (arrows in central image), bounded by organic membranes. Arrowheads of right image point to organic threads between fibers. (B, C) Lamello-fibrillar calcite of *Spirobranchus triqueter*. (B) Layers clearly marked by organic membranes (see zoomed views of framed areas). These disappear into external finely granular prismatic layer. (C) Detail of organic membrane between layers. Organic threads between calcite fibers indicated with arrowheads. (D, E) Lamello-fibrillar microstructure of middle cross-section of tube of *Serpula vermicularis*. (D) Note changing thicknesses of layers. Close-up view shows changes in orientation of fibers between layers and rotation of fibers inside central layer (white arrows). (E) View similar to close-up in D. (F, G) Longitudinal cross-sections of tube of *S. vermicularis*. Lamello-fibrillar layers have varied thicknesses and wedge out frequently

This procedure revealed the existence of relict calcite grains within the aragonite fibers close to the interface with the calcitic microstructure (particularly evident in Fig. 8A, B).

The crystallography of the spherulitic microstructure is shown in Fig. 9. The analysis was performed on a polished cross-section of *Spirobranchus giganteus*, at the boundary between the finely granular-prismatic calcite and the fibrous aragonite microstructures, located in the middle of the tube (Fig. 9A). The BC map (Fig. 9B, left) showed a better diffraction signal of the calcite grains (lighter areas) than of the fibrous aragonite. The phase map (Fig. 9B, right) corroborated the polymorph distribution (see legend). The

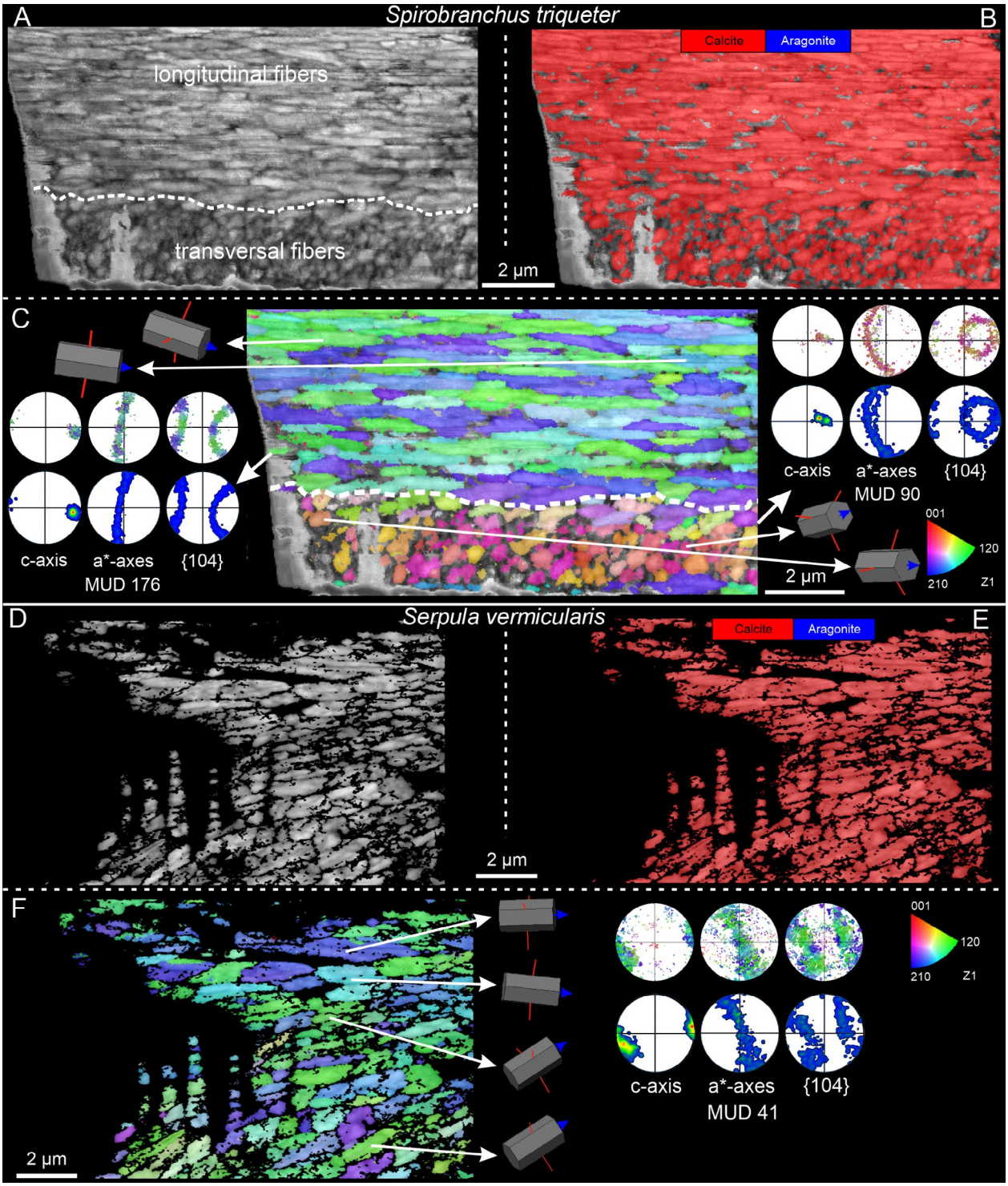

Fig. 6 EBSD analysis of lamello-fibrillar calcite of *Spirobranchus triqueter* (A-C) and *Serpula vermicularis* (D-F). (A) BC map. Contours of fibers easily recognizable. They arrange longitudinally at top and transversely at bottom. (B) Phase map indicates entire structure is made of calcite (see legend). (C) IPFz map shows that fibers' c-axis is co-oriented within each layer (note similar colors). PFs for each layer show strong axial texture, where calcite c-axis is fiber axis, aligned in elongation direction of fibers (as also indicated by unit cells). High MUD values of two superposed layers (176 and 90) indicate high co-orientations. (D) BC map. Some areas of left side (in black) not indexed due to damage to lamella. (E) Phase map. Red color indicates calcitic nature of the sample. (F) IPFz map. Purple-green colors show that fibers were cut approximately parallel to c-axis. Fiber spread is evident (indicated by cell lattices). PFs show axial texture, in which calcite c-axis is fiber axis, aligned in elongation direction of fibers (see also unit cells). MUD value (41) well below those of *S. triqueter* (see C). Color triangle is orientation color key

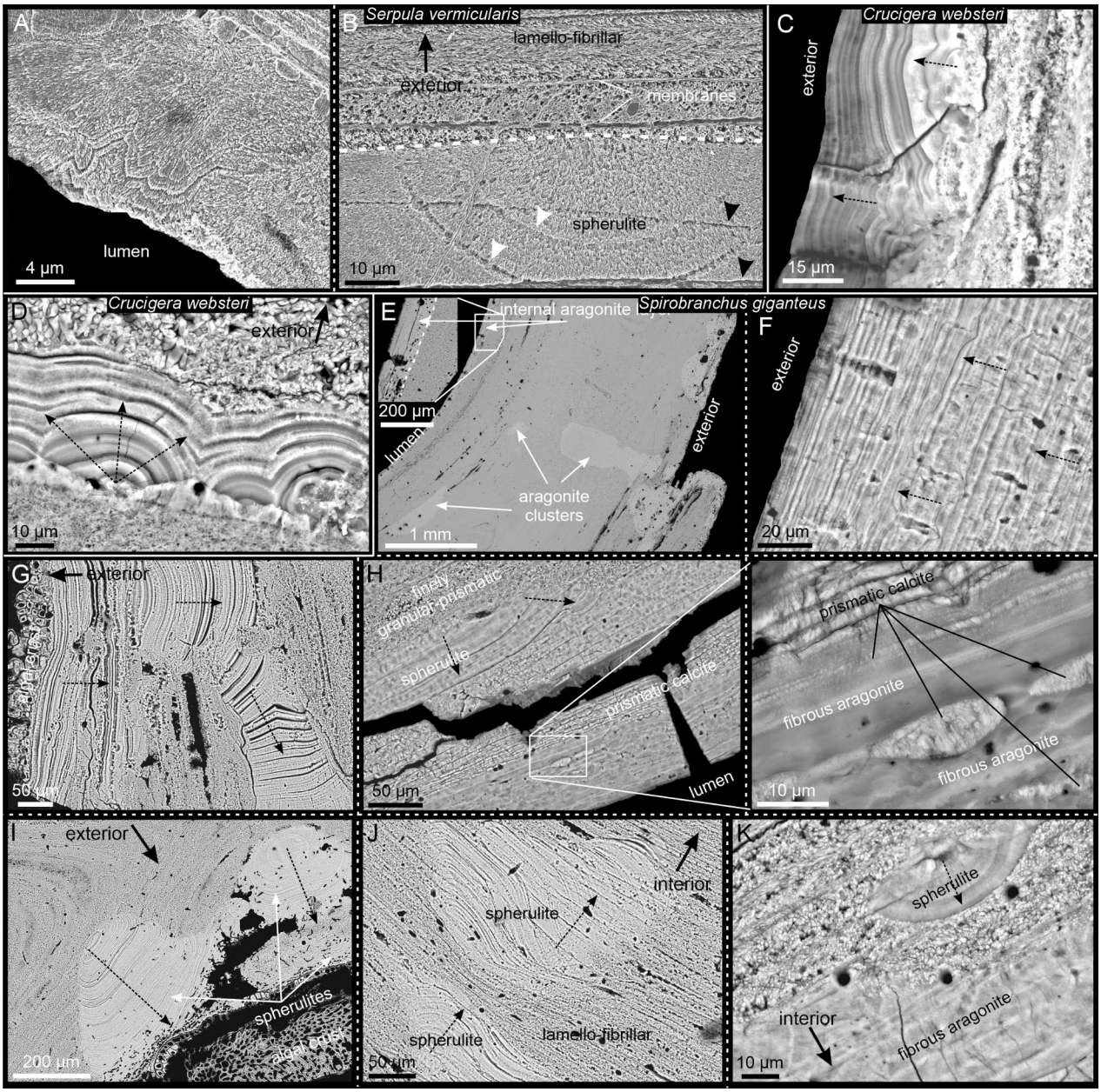

Fig. 7 Fibrous aragonite microstructure. (A, B) Spherulites in *Serpula vermicularis*. (A) Coalescing aggregates of fibrous aragonite with angular outlines. Growth lines visible. (B) Spherulite in interior of tube, underlying lamello-fibrillar layers. Its concentric growth lines (white arrowheads) extend across relict organic membranes of lamello-fibrillar calcite (black arrowheads). (C, D) Spherulitic aragonite of *Crucigera websteri*. (C) Outermost layer made of spherulites fusing outward and forming roughly continuous layer. (D) Cluster of spherulites growing toward exterior. (E-K) Fibrous aragonite of *Spirobranchus giganteus*. (E) Fibrous internal layer and scattered spherulitic clusters of tube cross-section. Aragonite discerned by lighter contrast. (F) Internal discontinuous layers growing toward exterior. Note borings crossing growth lines. (G) Outer fibrous layer growing toward interior and diverting laterally. Note algal crust. (H) Innermost layer made of prismatic calcite and fibrous aragonite. Fibrous aragonite alternates with finely granular-prismatic calcite (see magnification). (I) Spherulites scattered within external area of tube overgrown by calcareous algae. (J) Sectioned fibrous spherulites intersecting lamello-fibrillar layers. Boundaries of latter continue into spherulites. (K) Spherulite and irregular layer growing within lamello-fibrillar material, close to tube interior. Growth lines of aragonitic structures intersect vestigial membranes between lamello-fibrillar layers, in turn crossed by borings. Broken arrows indicate growth directions

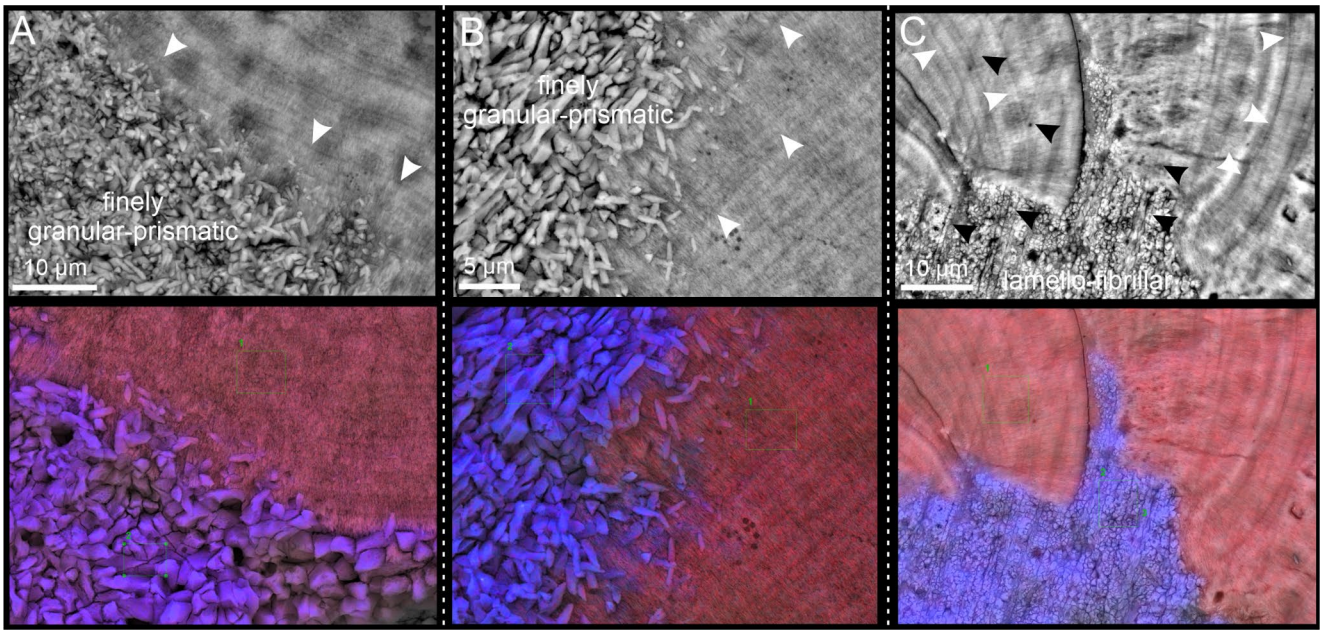

Fig. 8 EDX analysis of interface between calcite and aragonite spherulites in *Spirobranchus giganteus*. (A-C) SEM views of interfaces (top) and respective EDX maps (red = Ca^{2+}; blue = Mg^{2+}) (bottom). White arrowheads indicate growth lines of aragonite spherulites. Black arrowheads (C) point to relict organic membranes continuing into spherulites

EBSD map (IPFz maps, Fig. 9C) revealed a predominance of green-orange colors for the fibrous aragonite and a wider variety of colors (orientations) for the granular-prismatic calcite, suggesting that the former was better co-oriented. The cell lattices and pole figures for the aragonite fibers (Fig. 9C, right) indicated that their c-axes were parallel to their long axis. The fibrous aragonite had a moderate axial texture (MUD value 65), with the c-axis as the fiber axis, while the calcite grains-prisms were randomly oriented (MUD value 17; Fig. 9C, left).

Discussion

Microstructures and mineralogy

We identified three different microstructures in seven species of serpulids: granular-prismatic calcite, lamello-fibrillar calcite, and fibrous aragonite. For each one, we determined their morphological details, distribution within the tube, and mineralogy (Figs. 1, S1 and S2). The lamello-fibrillar calcite forms the bulk of the tube structure in all the samples studied, except in *Serpula crenata*. The granular-prismatic calcite and the fibrous aragonite are relegated to internal or external layers or appear in the form of ubiquitous (sometimes large) clusters within the tube cross-section. The calcite of the serpulids consistently occurs as medium to high Mg calcite (Smith et al. 2013), also confirmed by our analyses (> 10% of $MgCO_3$; Fig. S1C, D).

Our observations allow us to conclude that only the lamello-fibrillar and external prismatic microstructures are primary (i.e. directly secreted by the serpulid), whereas the rest results from processes of replacement-recrystallization of these original microstructures. Below, we describe the features which allow us to distinguish between original and replacement microstructures:

A. Original microstructures

External prismatic layers

1. They have consistent orientations perpendicular to the external surface (Figs. 1A, B and 2A–D).
2. With growth, there is competition for space, such that some elements become thicker at the expense of others (Grigor'ev 1965; Rodríguez-Navarro and García-Ruiz 2000) (Figs. 1B and 2A–C) and the aggregate becomes better co-oriented (e.g. increasing MUD values in Fig. 3D).
3. Growth lines are flat and continuous across the different crystals, indicating the existence of an epithelium lining the growth surface (Fig. 2A, D).

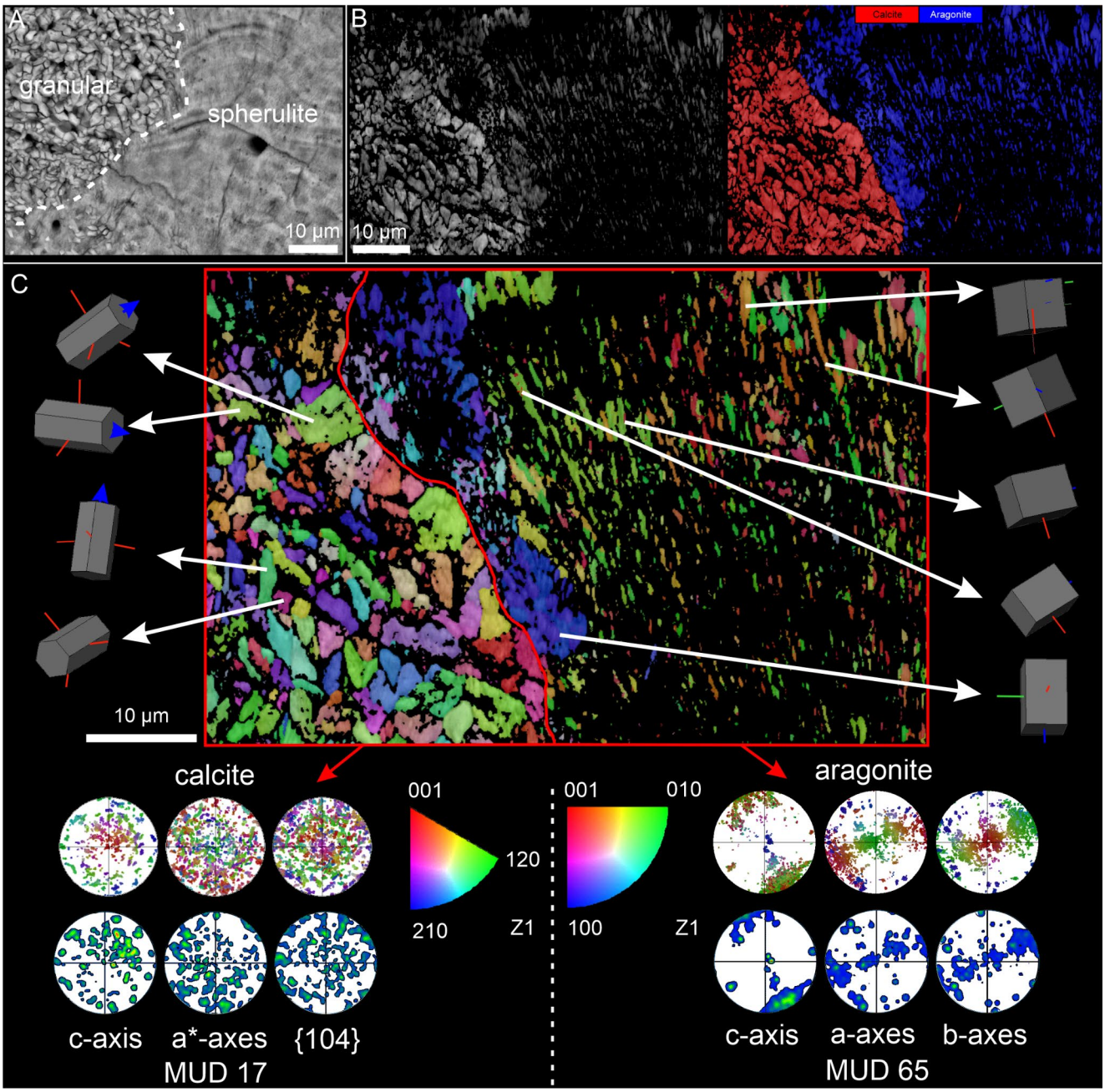

Fig. 9 EBSD analysis of spherulitic aragonite of *Spirobranchus giganteus*. (A) SEM image of border between granular-prismatic calcite and fibrous aragonite, similar to region analyzed in B to C. (B) BC map (left) shows stronger EBSD diffraction signal for calcite (lighter grey). Phase map (right) indicates distribution of calcite and aragonite (see legend). (C) IPFz map shows higher variety of colors for calcite grains than for aragonite fibers. Large grains of aragonite unrelated to spherulite (blue/purple in color) appear at boundary between microstructures. The PFs show a loose texture for calcite, and a moderate axial texture for aragonite, with c-axis as fiber axis, aligned in elongation direction of fibers (see unit cells). Co-orientation of aragonite concurs with relatively high MUD value (65), whereas near absence of orientation of calcite grains is indicated by low MUD value (17). Color triangle is orientation color key

Lamello-fibrillar layers

4. They constitute well-defined and relatively continuous layers parallel to the growth surface (Figs. 1A, C and 5).
5. Homogeneous dimensions and co-orientation of the constituent fibers within single layers (parallel to the intervening membranes) (Figs. 1C and 5A, C–E, G).
6. Presence of organic membranes between layers, together with minor organics between fibers (Fig. 5A, B).

In the lamello-fibrillar and the external prismatic layers, these features are consistent across the different species.

B. Secondary (replacement) microstructures

Secondary granular-prismatic materials

1. Prisms with rhombohedral endings enclosed within or forming part of the external primary prismatic layers. In these instances, the growth lines change from flat to angular. This indicates that the growth surfaces were not bounded by a secretory epithelium (Fig. 2C, D).
2. Small intra- or extra prismatic grains associated with the same external layers, at any growth stage (Fig. 2B, C). If they were original, they should be interpreted as new crystallization nuclei. Nevertheless, in columnar prismatic materials growing by crystal selection and competition, there is no opportunity for new crystals to appear (Stevens et al. 2017; Crippa et al. 2020a, b).
3. Highly irregular internal layers or clusters of coarse prisms or grains that laterally continue into lamello-fibrillar layers (Fig. 2F–I). Within these layers, the prismatic units have varied orientations and intersect with what seem to be remnants of organic membranes, similar and continuous with those separating the lamello-fibrillar layers. The membranes clearly did not belong to the prismatic layers but to the previous lamello-fibrillar layers (Fig. 2F, I).
4. Associated with the immediately previous instance, prismatic grains may form spherulitic arrangements which nucleate on the relict organic membranes (Fig. 2G). In addition to the membranes predating the calcitic grains, this arrangement indicates centrifugal growth, while in primary materials, growth must always proceed toward the interior of the tube.
5. The secondary grains sometimes fuse, producing either isolated aggregates (Fig. 2K), or spherulitic and concretional structures (Fig. 2L) without defined growth directions, which is contrary to primary materials.
6. In some cases, much thinner scattered or clustered fibers still cooriented within the different layers are present (Fig. 2L, M). We interpret them as remains of the original lamello-fibrillar microstructure being replaced by granular-prismatic materials.

Fibrous aragonite

1. The shapes of the growth surfaces of spherulites do not conform to the shape of the overall growth surface of the tube (Fig. 7). In some instances, according to the convexity of the growth lines, growth is inferred to proceed toward the tube's exterior (Fig. 7C, D, F, I) or interior (Fig. 7A, B, G, H, J, K). In any case, the growth fronts of the fibrous aragonite indicate that it was invading previous calcitic microstructures, either primary (Fig. 7B, G, I–K) or secondary (Fig. 7H). In high magnification, relict grains, either from the original or secondary calcitic microstructures, persist within the advancing aragonite spherulite (Fig. 8).
2. Organic membranes of the lamello-fibrillar microstructure continue as ghosts into the spherulites (Figs. 7B, H and I–K and 8C), which is indicative of replacement of the lamello-fibrillar microstructure by aragonite.

All the above features clearly indicate that the fibrous aragonite comes from replacement of the previous calcitic microstructures.

In all species analyzed, and independently of the microstructures previously described in the literature, only the lamello-fibrillar microstructure and the non-secondary granular-prismatic microstructures described above are original, while the rest are replacement microstructures.

A summary of the different instances in which replacement microstructures develop is provided in Fig. 10.

According to our observations, the primary microstructures may be replaced by either secondary calcite (Fig. 2F, G, I) or, directly, by aragonite (Fig. 7B, G, H–K). Transformation of the secondary calcite into aragonite has also been observed (Fig. 7H). We suggest that the replacement is likely induced by the high solubility of the primary high-Mg calcite and must occur via dissolution-recrystallization processes (Morse and Mackenzie 1990). This process would favor the crystallization of less soluble calcites (i.e., with slightly lower Mg contents), with the consequent accumulation of Mg^{2+} at the transformation interface. At some point, Mg^{2+} concentration may inhibit the formation of calcite and promote the precipitation of aragonite, which does not incorporate Mg^{2+} (see EDX maps in Fig. 8) (Burton and Walter 1987; Morse et al. 1997). This theoretical sequence

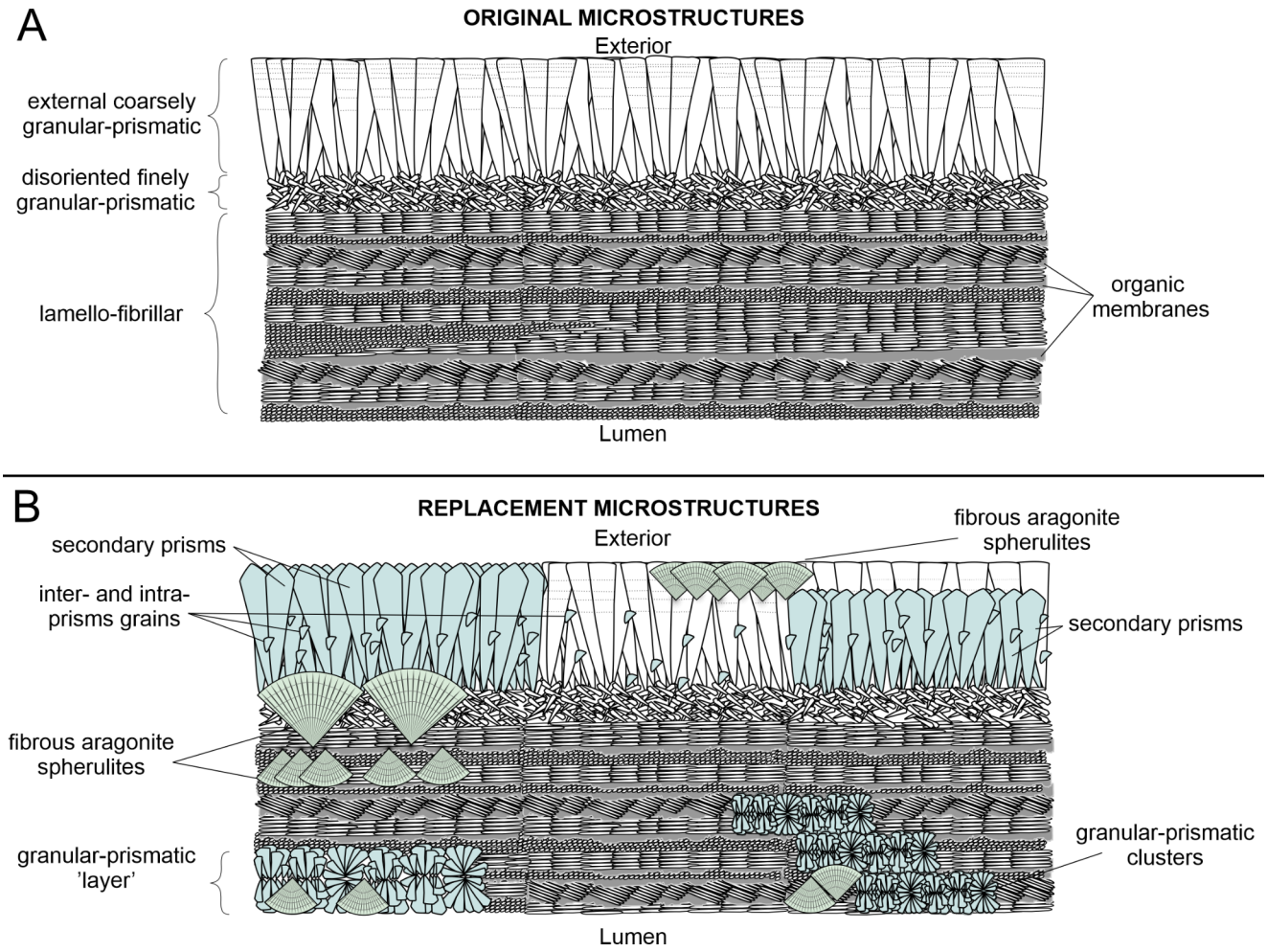

Fig. 10 Schematic representation of serpulid tube cross-section, with indication of original microstructures, before (A) and after (B) replacement by secondary microstructures. These are indicated in either pale blue (calcite) or green (aragonite)

can vary depending on local conditions, and aragonite could be produced directly, without the need for a secondary Mg calcite precursor.

Regarding the timing of substitution, there are two possibilities: (1) Since the studied specimens were collected alive, replacement processes happened in vivo. Out of the studied species, lifespan data were only provided for *Spirobranchus giganteus*, which usually lives > 10 years, but can live up to 40 years (Nishi and Nishihira 1996), and large *Serpula vermicularis*, which could be about 8 years old (Sanfilippo et al. 2013). In this case, replacement occurred in a matter of a few years.(2) Alternatively, replacement might have occurred during preservation of the specimens in 70% ethanol, for decades in some cases (see collection dates in Table 1). Stolarski et al. (2024) described post-mortem recrystallization of American lobster gastroliths preserved in an ethanol/water (9:1) medium for 30 d. The original amorphous calcium carbonate (ACC) plus amorphous calcium phosphate (ACP) recrystallized into calcite across a well-defined transformation front and with a fixed polarity (starting from the most recently formed end). Our material shows features different from those described by Stolarski et al. (2024), which suggest a different origin: (1) The original mineralogy of serpulid tubes was high-Mg calcite, instead of the less stable ACC + ACP of gastroliths; (2) in several cases in which replaced tube portions were overgrown by calcareous algae (high-Mg calcite) (Fig. 7G, I), no replacement of the calcified cell walls of the alga was observed (e.g. Figure 11A, B). (3) Borings produced by endolithic organisms sometimes crossed replacement microstructures (Figs. 2G, J and 7F, I–K). They clearly intersected the growth lines of the replacement fronts, instead of these adapting to the borings (Figs. 7F and 11C–E). (4) Replacement may initiate multiple times within a single tube, at any place within the tube, usually far from contact with the preserving solution, and progress either interiorly or exteriorly (Figs. 2F, K and 7A–D, F–K). Based on this evidence, we favor the in vivo replacement hypothesis, however we cannot discard the

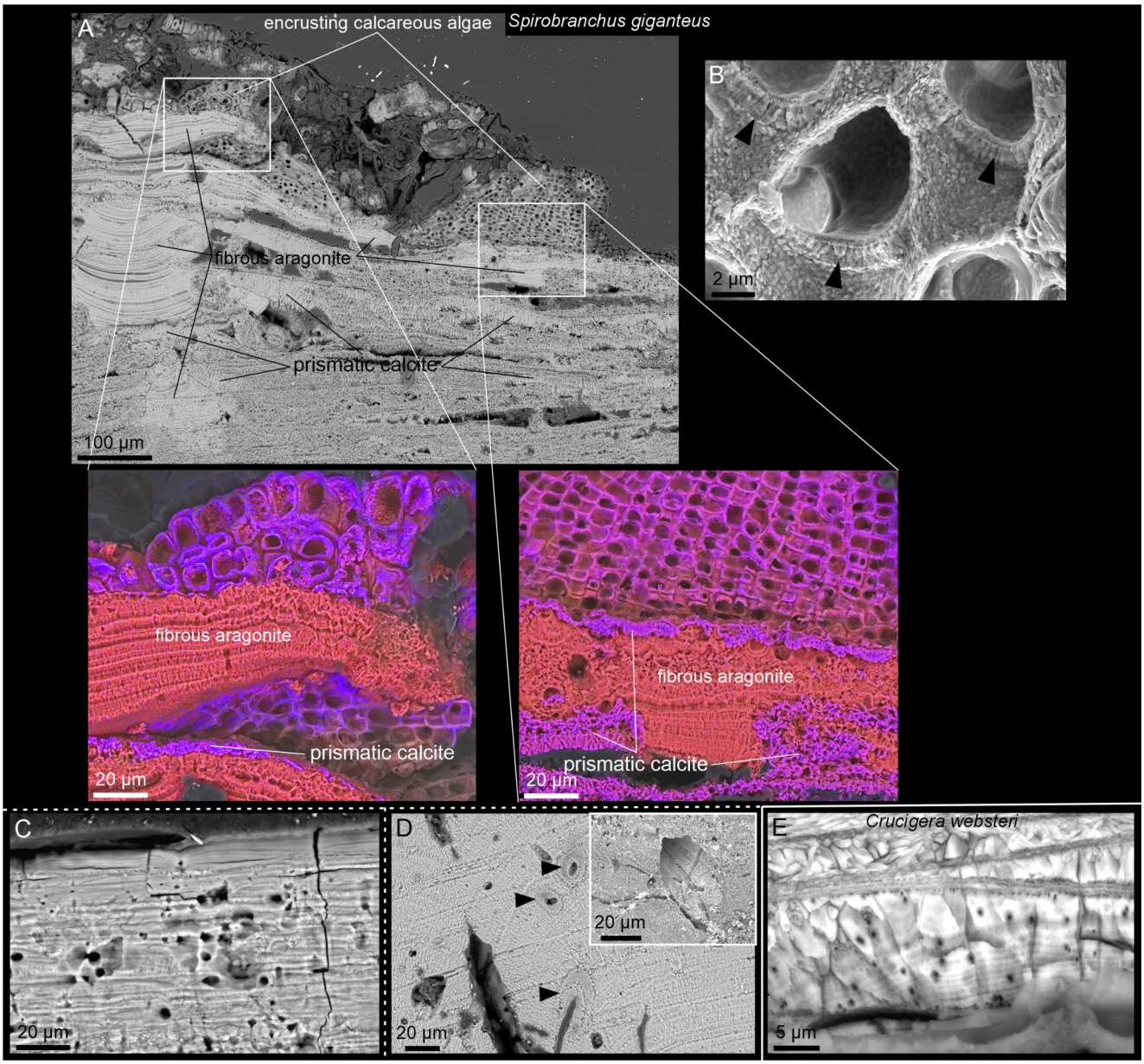

Fig. 11 Relationship of replacement microstructures with encrusters and borers. (A) View of tube of *Spirobranchus giganteus* encrusted by calcareous algae. Two EDX maps show that high-Mg calcite mineralogy (Mg^{2+} in blue) of algae is preserved, while serpulid tube has been replaced by either aragonite (devoid of Mg^{2+}, only Ca^{2+}, in red) or prismatic high-Mg calcite. (B) Detail of algal cells showing preservation of original, finely prismatic calcite of walls. (C, D) Variously sized borings in fibrous aragonite of *S. giganteus*. They cut both vestigial membranes and growth lines of aragonitic spherulites. Some borings have been secondarily partly filled with aragonite (arrowheads in B). Inset in B is large boring cutting through growth increments of spherulite. (E) Tiny borings in prismatic calcite of *Crucigera websteri*, cutting growth lines of prisms

"in jar" replacement possibility. The origin of the observed replacement processes will be investigated in detail in the future.

Growth patterns of the external prismatic and lamello-fibrillar layers

Considering that in serpulids, secreting glands, of both calcium carbonate and organic matter, are principally located in the folds of the peristomial collar, just beneath the radiolar crown (Hedley 1956), the deposition of new material occurs when the serpulid is in feeding mode (with the radiolar crown protruding outwards). At this point, the collar folds would be close to the edge of the tube, facilitating the addition of new material. The secretion of a new layer would stop each time the serpulid retracted inside the tube.

The distribution of growth lines of the primary external prismatic layers indicates that growth proceeds with the addition of closely spaced (submicron thick) growth increments (Fig. 2A, D). The flat, parallel, and continuous growth lines across the prisms mark the positions where the soft body adhered to the tube's growth surface to continue calcification. This pattern is similar to that found in other calcifying invertebrates, such as molluscs, brachiopods, and corals.

On the contrary, in the lamello-fibrillar microstructure, we did not find any evidence of growth lines within the layers, despite the different preparation protocols. The only evidence of periodicity was constituted by the organic membranes delineating the lamello-fibrillar layers (Fig. 5). Accordingly, we assume that these membranes correspond to the different growth episodes and delineate the contour of the mineralizing epithelium (the collar fold). This distribution pattern is suggestive of rather episodic growth, with increments of a few microns to several tens of microns.

To reconcile the relatively continuous growth of the external prismatic layer with the seemingly episodic growth of the lamello fibrillar layers, we envisage two possibilities: (1) Mineralization of the lamello-fibrillar layer takes place continuously, with the addition of sublayers one to several fibers thick; when the layer is complete, secretion of the organic membrane takes place (Fig. 12A). (2) The serpulid isolates a space with a new membrane at a distance from the previous membrane, enriched in the mineralization precursors of the calcitic fibers; mineralization of a fresh lamello-fibrillar layer takes place at once within this space (Fig. 12B). Whatever the exact process, this growth mode leads to the production of the characteristic pattern of unequal, sometimes slightly offset, growth wedges of lamello-fibrillar material (Fig. 5).

Other biocalcifiers, such as molluscs, bryozoans or brachiopods, can control the chemistry of the precipitation medium and the production of particular mineral phases (low-Mg calcite, aragonite). This is likely due to the fact that this occurs in a very narrow space (much less that one micron thick) between the mantle cells and the shell growth surface, called the extrapallial space (Nielsen and Pedersen 1979; Checa et al. 2014; Simonet Roda et al. 2019). This is isolated from the environment by an organic membrane, the periostracum in molluscs and brachiopods, and the cuticle in bryozoans. Serpulids, conversely, lack such an isolating membrane, and the growing edge of the tube is exposed to the environment, particularly when the worm is retracted inside its tube. This could explain the high-Mg calcite mineralogy of the serpulid microstructures, whose original microstructures are particularly prone to replacement processes, as explained above.

Assimilation of the plywood structure of the lamello-fibrillar calcite to a chiral nematic liquid crystal phase

The characteristic plywood arrangement of the lamello-fibrillar material, made of co-oriented fibers that twist their orientation across successive layers, is known as a "chevron pattern" (Weedon 1994). It was initially explained as being induced by swirling movements of the collar folds, which mold the material (still in a slurry state) through forward and backward applications before hardening (also Weedon 1994). However, this hypothesis fails to explain three critical issues: (1) how traction forces induce fiber orientations, (2) why the fibers achieve co-orientation across the whole thickness of a single layer, made of many superposed, co-oriented fibers (Fig. 5), and, as we reveal here, (2) how the crystallographic c-axis becomes co-oriented with the long axis of the fibers (Figs. 6, S5 and S7). Out of Hedley's hypothesis, no specific mechanism has been proposed to explain the plywood-like arrangement of the lamello-fibrillar calcite.

The changing orientation of fibers across the different layers is reminiscent of the plywood structures of many organic fibrous biocomposites in plants and animals (Neville 1993). Many such cases have been interpreted as resulting from a process of liquid crystallization, in particular, from the formation of the so-called cholesteric or chiral-nematic phase. In this phase configuration, polar nanofibers or molecules arrange in planes, and the fibers in each plane are parallel to each other and slightly rotated with respect to those of the contiguous plane. After a certain distance (called pitch), the orientation of the fibers becomes the same. In other instances, the change in orientation is abrupt, resulting in superposed lamellae of fibers with marked differences in orientation.

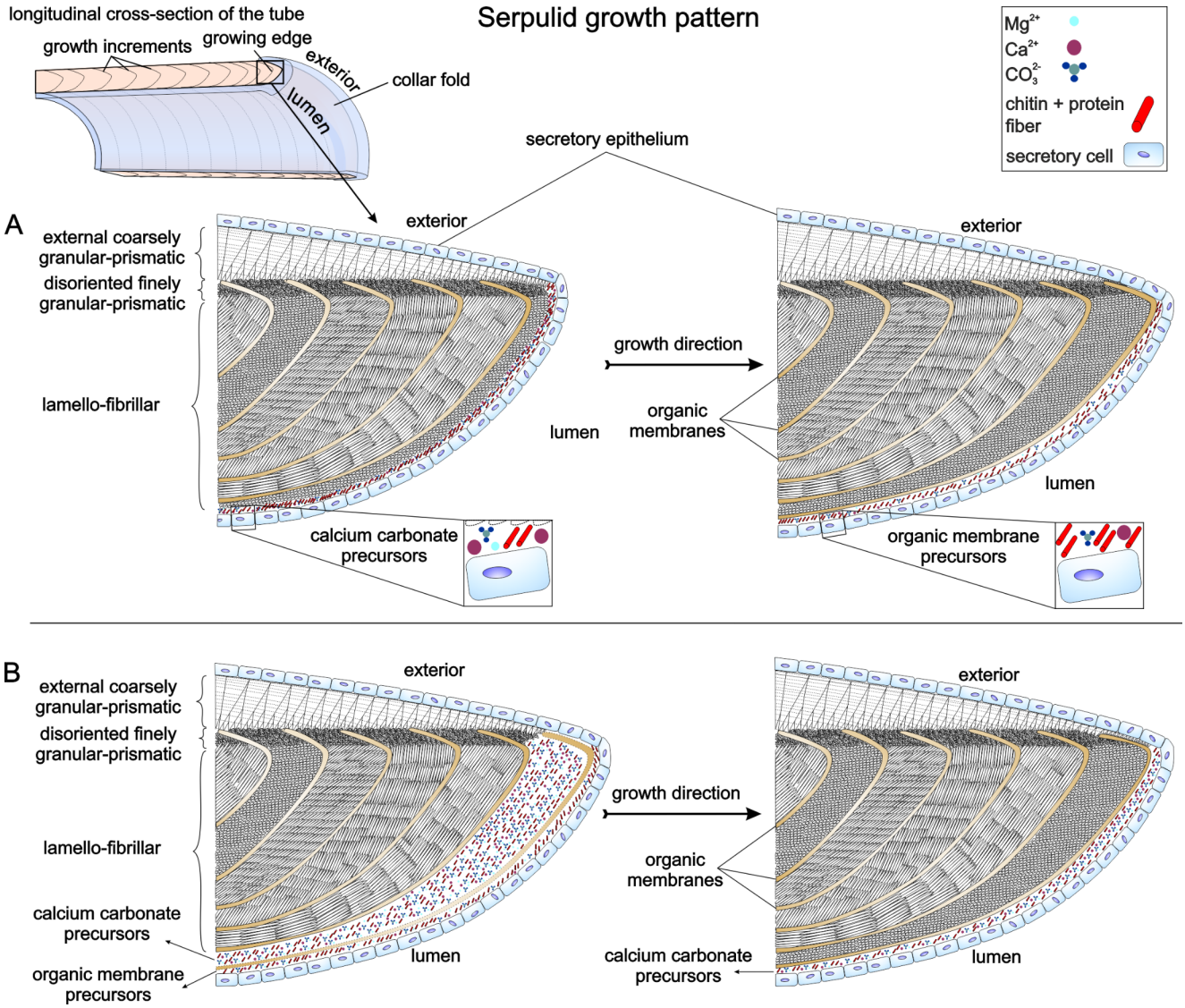

Fig. 12 Two possible growth modes for outer granular-prismatic and lamello-fibrillar microstructures. The top left sketch is a longitudinal section through tube wall and its relation to soft part. Secreting epithelium is collar fold. (A) Both granular-prismatic and lamello-fibrillar microstructures grow continuously toward tube exterior and interior, respectively. When lamello-fibrillar layer is complete, it is covered by organic membrane. (B) While granular-prismatic layer grows continuously toward external surface, space corresponding to the future lamello-fibrillar layer is filled with precursor components and sealed by membrane. Subsequently, mineralization of enclosed space takes place at once. In both cases (A and B), chitin + protein fibers organize as cholesteric liquid crystal phase and calcite grows by oriented nucleation

The most archetypal example of biological plywood materials attributed to cholesteric liquid crystallization is the arthropod exoskeleton, consisting of α-chitin + protein fibers (Bouligand 1972; Neville 1993). In molluscs (β-chitin + protein), similar patterns have been recognized in the periostracum of some gastropods (Hunt and Oates 1984), the squid pen (Levi-Kalisman et al. 2001), the chambers and septa of *Sepia* (Checa et al. 2015), and the septa of *Spirula* (Checa et al. 2022; Griesshaber et al. 2023). In all these instances, growth proceeds with the addition of successive layers. This is the opposite of in vitro-formed liquid crystals, in which all layers develop at once from a suspension.

The plywood structures of *Sepia* and *Spirula* are calcified with aragonite but there is no correspondence between the crystallographic c-axes of aragonite (perpendicular to the layers; Griesshaber et al. 2023) and the organic fibers of chitin protein (parallel to the layers). If we assimilate the formation of the lamello-fibrillar microstructure of serpulids to a liquid crystallization process, the calcite should nucleate onto previous organic fibrils, with its c-axis parallel to the long axis of the fibers (see EBSD data; Figs. 6, S5 and S7). This would constitute a unique case of oriented

nucleation. The putative fibers would be made of chitin (in its β-polymorph; Hunt and Oates 1984; Chamoy et al. 2001; Hausen 2005; Merz 2015; Choi et al. 2022) and proteins, two components we have identified within the tubes with FTIR (Fig. 8) (see also Tsurkan et al. 2021). We do not know if intra-layer growth proceeds sequentially (i.e. layer by layer, as in the previous biological examples) or all at once (see previous section). Unfortunately, we have not yet identified the organic precursor scaffold of the lamello-fibrillar material. Further research will be done in this area.

Conclusions

1. We identified three different microstructures: granular-prismatic calcite, lamello-fibrillar calcite, and fibrous aragonite. For each one, we characterized their distribution, mineralogy, and crystallography.
2. The granular-prismatic microstructure may be present either as (1) an outer layer of long prisms perpendicular to the external surface, or as (2) ubiquitous clusters or discontinuous layers in different parts of the tube cross-section.
3. The lamello-fibrillar microstructure has a plywood structure of thin fibers arranged in successive layers separated by membranes. It is found in the central and internal parts of the tube.
4. The fibrous aragonite usually forms spherulites and appears as discontinuous layers or clusters at any location in the tube.
5. Serpulid tubes incorporate a high amount of organic matter, consisting primarily of chitin plus protein. Calcite is always medium to high Mg calcite (> 10%).
6. From the crystallographic viewpoint, the calcitic external prismatic and lamello-fibrillar layers, and the fibrous aragonite present an axial texture, with either the calcite or the aragonite c-axis as the fiber axis. The lamello-fibrillar calcite displays the strongest texture. The long prisms of the external prismatic calcite become better co-oriented with growth, a characteristic indicative of competition for space.
7. Only the external prismatic and the lamello-fibrillar microstructures are secreted by the serpulid. All the other instances of granular-prismatic and fibrous aragonite microstructures result from the in vivo replacement of original microstructures. The fibrous aragonite can also replace the secondary calcite. Replacement is likely triggered by the high Mg^{2+} content of the original calcites.
8. The external granular-prismatic layer exhibits continuous growth, while the lamello-fibrillar layers grow either: (1) by continuous addition of sublayers one to several fibers thick, until, upon completion of the layer, an organic membrane is secreted; or (2) by isolating a space sealed by a new membrane, where mineralization occurs at once.
9. We hypothesize that the plywood configuration of the lamello-fibrillar calcite occurs by the ordering of a precursor made of organic fibrils into a cholesteric liquid crystal phase. Subsequently, calcite would grow by oriented nucleation onto the organic fibrils. We have not identified the organic precursor.

Supplementary Information The online version contains supplementary material available at https://doi.org/10.1007/s00227-024-04552-w.

Acknowledgements We are particularly grateful to Dr. Harry ten Hove (Naturalis Biodiversity Center, Leiden) for providing material and all the pertinent information. We are grateful to the Academic Centre for Materials and Nanotechnology (ACMiN), AGH University, Krakow for providing technical support for sample preparation and analysis. In particular, Dr. Marta Gajewska helped in obtaining thin FIB lamellae for STEM-EBSD. We greatly appreciate the advice and review of Dr. Carlos Pimentel (Universidad Complutense de Madrid). We thank the reviewers for their dedicated and thorough reviews.

Author contributions CG and AGC conceptualized and designed the research. CG and AGC wrote the paper, with additions and revisions from the other authors. CG acquired data. KB contributed with FIB and EBSD analysis. ARN performed XRD Rietveld refinement. OV provided all the samples analyzed. All authors approved the final version of the manuscript.

Funding CG, ARN and AGC were funded by Projects PID2020 116660GB-I00 and PID2023-146394NB-I00 (Spanish Ministry of Science, Innovation and Universities: MICIU/AEI/https://doi.org/10.13039/501100011033). Additional financial support was obtained through the Research Project PCM 00092 (Consejería de Economía, Innovación, Ciencia y Empleo, Junta de Andalucía), and the Unidad Científica de Excelencia UCE-PP2016-05 of the University of Granada. CG and AGC were also funded by the Research Group RNM363 (Consejería de Economía, Innovación, Ciencia y Empleo, Junta de Andalucía). KB was supported by the program "Excellence Initiative—Research University" for the AGH University of Krakow.

Data availability The data sets generated during and/or analyzed during the current study are available from the corresponding author upon reasonable request.

Declarations

Ethical approval This study was conducted using invertebrate shells, for which ethical approval was not required.

Conflict of interest The authors declare no competing financial or non-financial interests.

Open Access Open access was funded by Project PID2020 116660GB-I00 (MICIU/AEI/10.13039/501100011033).

References

Badou A, Pont S, Auzoux-Bordenave S, Lebreton M, Bardeau J-F (2022) New insight on spatial localization and microstructures of calcite-aragonite interfaces in adult shell of *Haliotis tuberculata*: investigations of wild and farmed abalones by FTIR and Raman mapping. J Struct Biol 214:107854. https://doi.org/10.1016/j.jsb.2022.107854

Bouligand Y (1972) Twisted fibrous arrangements in biological materials and cholesteric mesophases. Tissue Cell 4:189–217. https://doi.org/10.1016/S0040-8166(72)80042-9

Buckman JO (2015) An overview of the tube fabric of *Pomatoceros* (Polychaeta, Serpulidae), illustrated by examples from the British Isles. Zool Anz 259:54–60. https://doi.org/10.1016/j.jcz.2014.11.005

Burton EA, Walter LM (1987) Relative precipitation rates of aragonite and Mg calcite from seawater: temperature or carbonate ion control? Geology 15:111–114. https://doi.org/10.1130/0091-7613(1987)15<111:RPROAA>2.0.CO;2

Chamoy L, Nicolaï M, Ravaux J, Quennedey B, Gaill F, Delachambre J (2001) A novel chitin-binding protein from the vestimentiferan *Riftia pachyptila* interacts specifically with β-chitin: Cloning, expression, and characterization. J Biol Chem 276:8051–8058. https://doi.org/10.1074/jbc.M009244200

Chan VBS, Li C, Lane AC, Wang Y, Lu X, Shih K, Zhang T, Thiyagarajan V (2012) CO_2-driven ocean acidification alters and weakens integrity of the calcareous tubes produced by the serpulid tubeworm, *Hydroides elegans*. PLoS ONE 7:e42718. https://doi.org/10.1371/journal.pone.0042718

Charles M, Faillettaz R, Desroy N, Fournier J, Costil K (2018) Distribution, associated species and extent of biofouling reefs formed by the alien species *Ficopomatus enigmaticus* (Annelida, Polychaeta) in marinas. Estuar Coast Shelf Sci 212:164–175. https://doi.org/10.1016/j.ecss.2018.07.007

Checa A, Salas C (2017) Treatise Online 93: part N, revised, 1, chap. 3: Periostracum and shell formation in the Bivalvia. Treat Online 1:1–51. https://doi.org/10.17161/to.v0i0.6650

Checa AG, Salas C, Harper EM, de Bueno-Pérez J D (2014) Early stage biomineralization in the periostracum of the 'living fossil' bivalve *Neotrigonia*. PLoS ONE 9:e90033. https://doi.org/10.1371/journal.pone.0090033

Checa AG, Cartwright JHE, Sánchez-Almazo I, Andrade JP, Ruiz-Raya F (2015) The cuttlefish *Sepia officinalis* (Sepiidae,Cephalopoda) constructs cuttlebone from a liquid-crystal precursor. Sci Rep 5:11513. https://doi.org/10.1038/srep11513ot

Checa AG, Grenier C, Griesshaber E, Schmahl WW, Cartwright JHE, Salas C, Oudot M (2022) The shell structure and chamber production cycle of the cephalopod *Spirula* (Coleoidea, Decabrachia). Mar Biol 169:132. https://doi.org/10.1007/s00227-022-04120-0

Choi H, Kim SL, Jeong M-K, Yu OH, Eyun S (2022) Identification and phylogenetic analysis of chitin synthase genes from the deep-sea polychaete *Branchipolynoe onnuriensis* genome. J Mar Sci Eng 10:598. https://doi.org/10.3390/jmse10050598

Coronado I, Fine M, Bosellini FR, Stolarski J (2019) Impact of ocean acidification on crystallographic vital effect of the coral skeleton. Nat Commun 10:2896. https://doi.org/10.1038/s41467-019-10833-6

Crippa G, Griesshaber E, Checa AG, Harper EM, Simonet Roda M, Schmahl WW (2020a) Orientation patterns of aragonitic crossed-lamellar, fibrous prismatic and myostracal microstructures of modern *Glycymeris* shells. J Struct Biol 212:107653. https://doi.org/10.1016/j.jsb.2020.107653

Crippa G, Griesshaber E, Checa AG, Harper EM, Simonet Roda M, Schmahl WW (2020b) SEM, EBSD, laser confocal microscopy and FE-SEM data from modern *Glycymeris* shell layers. Data Brief 33:106547. https://doi.org/10.1016/j.dib.2020.106547

Dos Santos HN, Neumann R, Ávila CA (2017) Mineral quantification with simultaneous refinement of Ca-Mg carbonates non-stoichiometry by X-ray diffraction, Rietveld method. Minerals 7:164. https://doi.org/10.3390/min7090164

Fischer R, Pernet B, Reitner J (2000) Organomineralization of cirratulid annelid tubes -fossil and recent examples. Facies 42:35–49. https://doi.org/10.1007/BF02562565

Griesshaber E, Checa AG, Salas C, Hoffmann R, Yin X, Neuser R, Rupp U, Schmahl WW (2023) Biological light-weight materials: the endoskeletons of cephalopod mollusks. J Struct Biol 215:107988. https://doi.org/10.1016/j.jsb.2023.107988

Grigor'ev DP (1965) Ontogeny of minerals. Israel Program for Scientific Translations, Jerusalem

Hausen H (2005) Comparative structure of the epidermis in polychaetes (Annelida). Hydrobiologia 535:25–35. https://doi.org/10.1007/s10750-004-4442-x

Hedley RH (1956) Studies of serpulid tube formation: I. The secretion of the calcareous and organic components of the tube by *Pomatoceros triqueter*. J Cell Sci 3:411–419

Hedley RH (1958) Tube formation by *Pomatoceros triqueter* (Polychaeta). J Mar Biol Ass 37:315–322. https://doi.org/10.1017/S0025315400023717

Hunt S, Oates K (1984) Chitin helicoids accompany protein helicoids in the periostracum of a whelk, *Buccinum*. Tissue Cell 16:565–575. https://doi.org/10.1016/0040-8166(84)90031-4

Jewett EB, Hines AH, Ruiz GM (2005) Epifaunal disturbance by periodic low levels of dissolved oxygen: native vs. invasive species response. Mar Ecol Prog Ser 304:31–44. https://doi.org/10.3354/meps304031

Kim Y, Caumon M-C, Barres O, Sall A, Cauzid J (2021) Identification and composition of carbonate minerals of the calcite structure by Raman and infrared spectroscopies using portable devices. Spectrochim Acta A 261:119980. https://doi.org/10.1016/j.saa.2021.119980

Kupriyanova EK, Vinn O, Taylor PD, Schopf JW, Kudryavtsev AB, Bailey-Brock J (2014) Serpulids living deep: calcareous tubeworms beyond the abyss. Deep-Sea Res I: Oceanogr Res Pap 90:91–104. https://doi.org/10.1016/j.dsr.2014.04.006

Kupriyanova EK, Hutchings P, Wong E (2016) A fully illustrated web-based guide to distinguish native and introduced polychaetes of Australia. Manag Biol Invasions 7:305–312. https://doi.org/10.3391/mbi.2016.7.3.10

Lacoste E, Gaertner-Mazouni N (2015) Biofouling impact on production and ecosystem functioning: a review for bivalve aquaculture. Rev Aquacult 7:187–196. https://doi.org/10.1111/raq.12063

Levi-Kalisman Y, Falini G, Addadi L, Weiner S (2001) Structure of the nacreous organic matrix of a bivalve mollusk shell examined in the hydrated state using cryo-TEM. J Struct Biol 135:8–17. https://doi.org/10.1006/jsbi.2001.4372

Lowenstam HA (1954) Factors affecting the aragonite: calcite ratios in carbonate-secreting marine organisms. J Geol 62:284–322. https://doi.org/10.1086/626163

Merz RA (2015) Textures and traction: how tube-dwelling polychaetes get a leg up. Invertebr Biol 134:61–77. https://doi.org/10.1111/ivb.12079

Montefalcone M, Oprandi A, Azzola A, Morri C, Bianchi CN (2022) Serpulid reefs and their role in aquatic ecosystems: a global review. Adv Mar Biol 92:1–54. https://doi.org/10.1016/bs.amb.2022.06.001

Morse JW, Mackenzie FT (1990) Geochemistry of sedimentary carbonates. Elsevier, Amsterdam

Morse JW, Wang Q, Tsio MY (1997) Influences of temperature and Mg:Ca ratio on $CaCO_3$ precipitates from seawater. Geology 25:85–87. https://doi.org/10.1130/0091-7613(1997)025<0085:IOTAMC>2.3.CO;2

Nelson KS, Liddy M, Lamare MD (2017) Embryology, larval development, settlement and metamorphosis in the New Zealand serpulid polychaete *Galeolaria hystrix*. Invertebr Reprod Dev 61:207–217. https://doi.org/10.1080/07924259.2017.1318183

Neville AC (1993) Biology of fibrous composites: development beyond the cell membrane. Cambridge University Press, Cambridge, UK

Nielsen C, Pedersen KJ (1979) Cystid structure and protrusion of the polypide in *Crisia*. Cyclostomata) Acta Zool 60:65–88. https://doi.org/10.1111/j.1463-6395.1979.tb00599.x

Nishi E, Nishihira M (1996) Age-estimation of the Christmas Tree worm *Spirobranchus Giganteus* (Polychaeta, Serpulidae) living buried in the coral skeleton from the coral-growth band of the host coral. Fish Sci 62:400–403. https://doi.org/10.2331/FISHSCI.62.400

Rashidi NA, Mohamed M, Yusup S (2012) The kinetic model of calcination and carbonation of *Anadara granosa*. Int J Renew Energy Res 2:497–503

Rodríguez-Navarro AB, García-Ruiz JM (2000) Model of textural development of layered crystal aggregates. Eur J Mineral 12:609–614. https://doi.org/10.1127/0935-1221/2000/0012-0609

Rodríguez-Navarro AB, Cabral de Melo C, Batista N, Morimoto N, Álvarez-Lloret P, Ortega-Huertas M, Fuenzalida VM, Arias JI, Wiff JP, Arias JL (2006) Microstructure and crystallographic texture of giant barnacle (*Austromegabalanus psittacus*) shell. J Struct Biol 156:355–362. https://doi.org/10.1016/j.jsb.2006.04.009

Rossbach FI, Casoli E, Beck M, Wild C (2021) Mediterranean red macro algae mats as habitat for high abundances of serpulid polychaetes. Diversity 13:265. https://doi.org/10.3390/d13060265

Sanfilippo R, Vertino A, Rosso A, Beuck L, Freiwald A, Taviani M (2013) *Serpula*-aggregates and their role in deep-sea coral communities in the southern Adriatic Sea. Facies 59:663677. https://doi.org/10.1007/s10347-012-0356-7

Simonet Roda M, Griesshaber E, Ziegler A, Rupp U, Yin X, Henkel D, Häussermann V, Laudien J, Brand U, Eisenhauer A (2019) Calcite fibre formation in modern brachiopod shells. Sci Rep 9:598. https://doi.org/10.1038/s41598-018-36959-z

Simonet Roda M, Griesshaber E, Angiolini L, Rollion-Bard C, Harper EM, Bitner MA, Milner Garcia S, Ye F, Henkel D, Häussermann V, Eisenhauer A, Gnägi H, Brand U, Logan A, Schmahl WW (2022) The architecture of recent brachiopod shells: diversity of biocrystal and biopolymer assemblages in rhynchonellide, terebratulide, thecideide and craniide shells. Mar Biol 169:4. https://doi.org/10.1007/s00227-021-03962-4

Smith AM, Riedi MA, Winter DJ (2013) Temperate reefs in a changing ocean: skeletal carbonate mineralogy of serpulids. Mar Biol 160:2281–2294. https://doi.org/10.1007/s00227-013-2210-z

Stevens K, Griesshaber E, Schmahl W, Casella LA, Iba Y, Mutterlose J (2017) Belemnite biomineralization, development, and geochemistry: the complex rostrum of *Neohibolites minimus*. Palaeogeogr Palaeoclimatol Palaeoecol 468:388–402. https://doi.org/10.1016/j.palaeo.2016.12.022

Stolarski J, Coronado I, Potocka M, Janiszewska K, Mazur M, Baronnet A, Cruz JA, Grauby O, Meibom A (2024) Post–mortem recrystallization of biogenic amorphous calcium carbonate guided by the inherited macromolecular framework. Sci Rep 14:17304. https://doi.org/10.1038/s41598-024-68037-y

Tanur AE, Gunari N, Sullan RMA, Kavanagh CJ, Walker GC (2010) Insights into the composition, morphology, and formation of the calcareous shell of the serpulid *Hydroides dianthus*. J Struct Biol 169:145–160. https://doi.org/10.1016/j.jsb.2009.09.008

ten Hove HA, Kupriyanova EK (2009) Taxonomy of Serpulidae (Annelida, Polychaeta): the state of affairs. Zootaxa 2036:1–126. https://doi.org/10.11646/zootaxa.2036.1.1

ten Hove HA, Van den Hurk P (1993) A review of recent and fossil serpulid reefs; actuopalaeontology and Upper Malm serpulid limestones in NW Germany. Geol Mijnbouw 72:23–67

Tilic E, Rouse GW, Bartolomaeus T (2021) Comparative ultrastructure of the radiolar crown in Sabellida (Annelida). Zoomorphology 140:27–45. https://doi.org/10.1007/s00435-020-00509-x

Tsurkan MV, Voronkina A, Khrunyk Y, Wysokowski M, Petrenko I, Ehrlich H (2021) Progress in chitin analytics. Carbohydr Polym 252:117204. https://doi.org/10.1016/j.carbpol.2020.117204

Vinn O (2009) The ultrastructure of calcareous cirratulid (Polychaeta, Annelida) tubes. Est J Earth Sci 58:153. https://doi.org/10.3176/earth.2009.2.06

Vinn O (2011) The role of an internal organic tube lining in the biomineralization of serpulid tubes. Carnets Géol https://doi.org/10.4267/2042/38798

Vinn O (2021) Biomineralization in polychaete annelids: a review. Minerals 11:1151. https://doi.org/10.3390/min11101151

Vinn O, ten Hove HA, Mutvei H (2008a) On the tube ultrastructure and origin of calcification in sabellids (Annelida, Polychaeta). Palaeontology 51:295–301. https://doi.org/10.1111/j.1475-4983.2008.00763.x

Vinn O, ten Hove HA, Mutvei H, Kirsimäe K (2008b) Ultrastructure and mineral composition of serpulid tubes (Polychaeta, Annelida). Zool J Linn Soc 154:633–650. https://doi.org/10.1111/j.1096-3642.2008.00421.x

Vinn O, Mutvei H, ten Hove HA, Kirsimäe EK (2008c) Unique Mg-calcite skeletal ultrastructure in the tube of the serpulid polychaete *Ditrupa*. N Jb Geol Paläont Abh 248:79–89. https://doi.org/10.1127/0077-7749/2008/0248-0079

Weedon MJ (1994) Tube microstructure of recent and jurassic serpulid polychaetes and the question of the Palaeozoic 'spirorbids'. Acta Palaeontol Pol 39:1–15

WoRMS Editorial Board (2024) World Register of Marine Species. Available from https://www.marinespecies.org at VLIZ. Accessed 2024-05-10. https://doi.org/10.14284/170

Xie Z, Wong N, Qian P, Qiu J (2005) Responses of polychaete *Hydroides elegans* life stages to copper stress. Mar Ecol Prog Ser 285:89–96. https://doi.org/10.3354/meps285089

Yin X, Griesshaber E, Checa A, Nindiyasari-Behal F, Sánchez-Almazo I, Ziegler A, Schmahl WW (2021) Calcite crystal orientation patterns in the bilayers of laminated shells of benthic rotaliid foraminifera. J Struct Biol 213:107707. https://doi.org/10.1016/j.jsb.2021.107707